Tectonophysics 617 (2014) 1–19

Contents lists available at ScienceDirect

Tectonophysics

journal homepage: www.elsevier.com/locate/tecto

Review Article

Global radially anisotropic mantle structure from multiple datasets: A review, current challenges, and outlook

Sung-Joon Chang [a,b,*], Ana M.G. Ferreira [a,c], Jeroen Ritsema [d], Hendrik J. van Heijst [e], John H. Woodhouse [f]

[a] School of Environmental Sciences, University of East Anglia, Norwich NR4 7TJ, UK
[b] Dept. of Geophysics, Kangwon National University, Chuncheon, Gangwon-do 200-701, South Korea
[c] Dept. of Earth Sciences, University College London, London WC1E 6BT, UK
[d] Dept. of Earth and Environmental Sciences, University of Michigan, Ann Arbor, MI 48109, USA
[e] Shell International Exploration and Production, Aberdeen AB15 9DL, UK
[f] Dept. of Earth Sciences, University of Oxford, Oxford OX1 3PR, UK

ARTICLE INFO

Article history:
Received 21 October 2013
Received in revised form 22 January 2014
Accepted 24 January 2014
Available online 1 February 2014

Keywords:
Radial anisotropy
Group velocity
Crustal corrections
Tomography
LPO
SPO

ABSTRACT

Since the 1960s seismologists have mapped anisotropy in the uppermost mantle, the mantle transition zone, and the D″ region. When combined with constraints from mineral physics and geodynamics, anisotropy provides critical information on the geometry of mantle flow. Here we review the theory, early work, recent tomographic models, and experimental constraints on radial anisotropy. We discuss current challenges in resolving radial anisotropy seismically. In particular, we show that it is highly beneficial to use multiple datasets in inversions for anisotropy, notably short-period group velocity data with strong sensitivity to the crust. We present a new whole-mantle model of radial anisotropy, based on surface-wave and body-wave travel time data, along with incorporated Moho perturbations. Our whole-mantle model shares common features with previous global models and is consistent with results from several high-resolution regional studies.

Contents

---

* Corresponding author at: Dept. of Geophysics, Kangwon National University, Chuncheon, Gangwon-do 200-701, South Korea.
E-mail address: sjchang@kangwon.ac.kr (S.-J. Chang).

0040-1951/$ – see front matter © 2014 Elsevier B.V. All rights reserved.
http://dx.doi.org/10.1016/j.tecto.2014.01.033

---

1. Introduction

Single-crystal olivines and pyroxenes, the main constituents of the Earth's upper mantle, are highly anisotropic. For example, shear-wave velocity in an olivine crystal can vary up to 20% depending on the axis of symmetry (e.g., Kumazawa and Anderson, 1969; Mainprice, 2007). However, in order to develop macro-scale seismic anisotropy large-strain deformation must align the minerals. Mantle flow can deform and align anisotropic minerals in a so-called lattice-preferred orientation (LPO). Therefore, the orientation, symmetry, and strength of seismic anisotropy can be extremely useful to constrain mantle convection.

Many studies have provided seismic evidence for azimuthal and radial anisotropy in the Earth's interior. Azimuthal anisotropy, where wave speed depends on the azimuth of propagation, was first recognized by Hess (1964) and is often studied through shear-wave splitting measurements. It is also referred to as horizontal transverse isotropy, given a horizontal symmetry axis in hexagonal symmetry. Azimuthal anisotropy and shear-wave splitting results have been reviewed by Silver (1996), Savage (1999), and Long (2013). In this review, we focus mainly on radial anisotropy in the Earth's mantle.

Radial anisotropy was first observed by Anderson (1961, 1965), Aki and Kaminuma (1963), and McEvilly (1964), who recognized that Rayleigh and Love wave dispersion cannot be explained by isotropic velocity profiles. Radial anisotropy is also known as polarization anisotropy or vertical transverse isotropy. Since there was a consensus on the presence of radial anisotropy in the uppermost mantle, the Preliminary Reference Earth Model (PREM; Dziewoński and Anderson, 1981), one of the most widely used 1-D seismic velocity models, incorporates radial anisotropy between the Moho (at 24.4 km depth) and a seismic discontinuity at 220 km depth. There have been some attempts to constrain the 3-D radially anisotropic structure of the mantle (e.g., Ekström and Dziewoński, 1998; Ferreira et al., 2010; Gung et al., 2003; Kustowski et al., 2008; Lekić and Romanowicz, 2011; Montagner and Tanimoto, 1991; Nataf et al., 1984; Panning and Romanowicz, 2006; Shapiro and Ritzwoller, 2002; Visser et al., 2008; Zhou et al., 2006) since the development of seismic tomography in the late 1970s (Aki et al., 1977; Dziewoński et al., 1977; Woodhouse and Dziewoński, 1984). However, large discrepancies still persist among the various 3-D radially anisotropic mantle models, in contrast with global 3-D isotropic models, which show a good level of agreement at least for long-wavelength structure in the upper mantle. The relatively slow progress in anisotropic tomography reflects the subtle effects of anisotropy on seismic waveforms, which cannot be easily separated from the effects of isotropic structure, notably in the crust and in the lowermost mantle (e.g., Ferreira et al., 2010; Kustowski et al., 2008; Panning et al., 2010).

In this paper, we review the theoretical background, the implications of radial anisotropy for interpretations based on mineral physics, and the development of 3-D radially anisotropic mantle models. We also compare results from regional studies of radial anisotropy with global 3-D radially anisotropic models and discuss synthetic tests to determine the sensitivities of various seismic data types to radial anisotropy. In particular, we explore current challenges and new strategies to better resolve radial anisotropy in the Earth's mantle. We present a new 3-D global radially anisotropic model, where we reduce the impact of the crust on the imaging of radial anisotropy in the mantle by incorporating short-period surface-wave group-velocity data as well as phase velocity and body-wave travel time data.

2. Theoretical background

Seismic anisotropy can be represented by an elastic tensor, which relates an applied stress to the resulting strain via Hooke's law as follows (e.g., Aki and Richards, 1980),

$$\tau_{ij} = c_{ijpq}\epsilon_{pq}, \tag{1}$$

where τ_{ij}, ϵ_{pq}, and c_{ijpq} are the stress, strain, and elastic tensor, respectively. Due to the following symmetries, the elastic tensor has 21 independent coefficients:

$$c_{jipq} = c_{ijpq}\left(\text{since}\,\tau_{ji} = \tau_{ij}\right) \tag{2}$$

$$c_{ijqp} = c_{ijpq}\left(\text{since}\,\epsilon_{qp} = \epsilon_{pq}\right) \tag{3}$$

$$c_{pqij} = c_{ijpq}. \tag{4}$$

The Eq. (4) is due to the first law of thermodynamics that the rates of mechanical work and heat flux are balanced with the increase rate of kinetic and internal energies; refer to Aki and Richards (1980) for its derivation. While all 21 coefficients are required to describe a medium with triclinic symmetry, the number of independent coefficients can be reduced if the medium itself is symmetric. Various symmetry classes are presented in Fig. 1. If the medium is isotropic, that is, a medium without variation of elastic parameters with direction, there are only two elastic coefficients (the Lamé constants: λ and μ) related to the compressional wave speed V_P and shear wave speed V_S by $(\lambda + 2\mu) = \rho V_P{}^2$ and $\mu = \rho V_S{}^2$, where, ρ is density.

A radially anisotropic medium has hexagonal symmetry with a vertical symmetry axis. This medium can be described by five independent elastic coefficients, which are traditionally called Love coefficients: A, C, F, L, and N (Love, 1927). They are related to seismic velocities as follows:

$$A = \rho V_{PH}^2 \tag{5}$$

$$C = \rho V_{PV}^2 \tag{6}$$

$$L = \rho V_{SV}^2 \tag{7}$$

$$N = \rho V_{SH}^2 \tag{8}$$

$$F = \frac{\eta}{A-2L}, \tag{9}$$

where, ρ is density, V_{PH} and V_{PV} are horizontally and vertically polarized P wave velocities, respectively, and V_{SH} and V_{SV} are horizontally and vertically polarized S wave velocities, respectively. η is a parameter relating to velocities at intermediate angle. *P*-wave and *S*-wave radial anisotropy can be described, respectively, as follows:

$$\phi = \frac{C}{A} = \frac{V_{PV}^2}{V_{PH}^2} \text{ and } \xi = \frac{N}{L} = \frac{V_{SH}^2}{V_{SV}^2}. \tag{10}$$

Since most tomographic studies of anisotropy in the upper mantle rely on surface wave data, they focus primarily on perturbations of isotropic *S* velocity and *S* radial anisotropy (e.g., Kustowski et al., 2008; Panning and Romanowicz, 2006). In order to keep the problem tractable, perturbations of V_{PH} and V_{PV} are scaled to perturbations of V_{SH} and V_{SV}, respectively (e.g., Anderson et al., 1968; Montagner and Anderson, 1989a; Robertson and Woodhouse, 1995), and lateral variations of η and density are often neglected (e.g., Kustowski et al., 2008) or remain proportional to *S* anisotropy and isotropic *S* velocity (e.g., Lekić and Romanowicz, 2011; Panning and Romanowicz, 2006). In addition to isotropic *S* velocity and *S* radial anisotropy, perturbations in the depth of the Moho (e.g., Woodhouse and Dziewoński, 1984) and mantle discontinuities (e.g., Gu et al., 2003; Kustowski et al., 2008) have also been included in inversions.

The inverse problem for radial seismic anisotropy can be written as follows:

$$\delta e = \int_0^a \left\{ K_S \delta S + K_\xi \delta \xi + K_d \delta d \right\} dr, \tag{11}$$

where δe is a measure of misfit between the data and theoretical calculations for a given reference model, *r* is the Earth's radius parameter, *a* is the total radius at the Earth's surface, and δS, $\delta \xi$, and δd indicate perturbations of isotropic *S* velocity, *S* radial anisotropy, and discontinuities with respect to the reference model. K_S, K_ξ, and K_d are depth sensitivity kernels with respect to isotropic *S* velocity, *S* anisotropy, and discontinuities, respectively. They relate the observations to the Earth's structure parameters, δS, $\delta \xi$, and δd.

There are many approaches to calculate sensitivity kernels. This includes ray theory for body waves (e.g., Woodhouse, 1981; Woodhouse and Girnius, 1982), the great-circle approximation for surface waves (e.g., Woodhouse and Dziewoński, 1984), nonlinear asymptotic coupling theory (NACT; Li and Romanowicz, 1996), and finite-frequency theory (e.g., Montelli et al., 2004; Zhou, 2009; Zhou et al., 2006). Ray-based methods are computationally efficient, and therefore useful for large-scale inversions with a large number of free parameters and diverse datasets. Hence, in this paper we focus mostly on global radial anisotropy imaging based on ray methods.

3. Implications of radial anisotropy

Lattice-preferred orientation (LPO) and shape-preferred orientation (SPO) are the two main mechanisms proposed to generate detectable seismic anisotropy in the Earth's mantle. LPO relates anisotropy to the preferential alignment of intrinsically anisotropic minerals (e.g., olivine) by deformation (e.g., Karato, 1998a; Nicolas and Christensen, 1987). SPO can be produced even if the materials are isotropic at fine scales. A stack of thin alternating layers with strong elastic contrasts, melts, or cracks can appear anisotropic at long wavelengths (Backus, 1962).

The Earth's mineralogy and anisotropic properties vary with depth, so it is necessary to consider the characteristics of LPO of each dominant mineral and possible origins for SPO for the various depth ranges within the Earth. In Sections 3.1, 3.2, and 3.3, we review the current understanding of LPO and SPO in the upper mantle, the mantle transition zone, and the lower mantle.

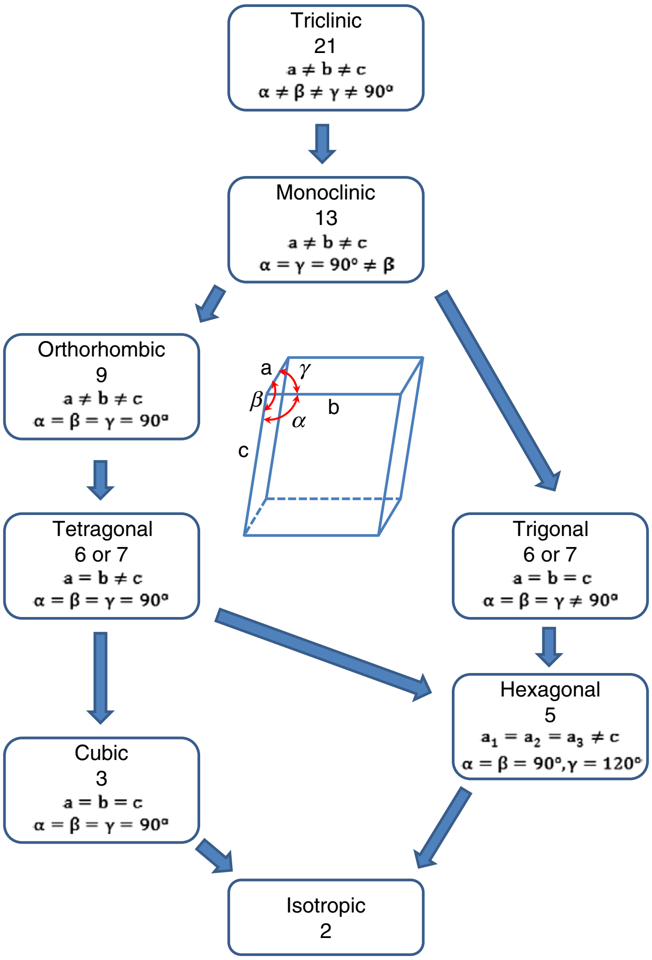

Fig. 1. Seven symmetry classes for anisotropic media. Each class has a number of required elastic coefficients and conditions.

3.1. Upper mantle

The dominant minerals in the upper mantle are olivine, orthopyroxene, clinopyroxene, and garnet. Garnet is nearly isotropic with single crystal V_S anisotropy of 1.3%, but olivine is very anisotropic with single crystal V_S anisotropy of 18% at ambient conditions (e.g., Mainprice, 2007). Previously it had been thought that *a*-axis of olivine is almost parallel to flow directions in any condition until the 2000s, which implies that regions with V_{SH} faster than V_{SV} are associated with horizontal flow, whereas regions with V_{SV} faster than V_{SH} are the loci of vertical mantle flow (e.g., Mainprice et al., 2000; Nicolas and Christensen, 1987). However, Jung and Karato (2001) found that LPO of olivine is sensitive to water content as well as to stress and temperature, so now olivine LPO is known to have five types: A, B, C, D, and E types, which have different directions of deformation in the same shear direction according to their slip systems (see Karato et al., 2008 for a detailed review). Dominant slip systems and radial anisotropy according to olivine LPO types are presented in Table 1. Olivine LPO changes from A type to E type, and from E type to C type with increasing water content. Recently, Ohuchi and Irifune (2013) reported that A-type olivine was developed under water-rich conditions with pressure and temperature corresponding to the deep upper mantle (>200 km), implying that $V_{SV} > V_{SH}$ observed beneath the East Pacific Rise may be attributed to vertical upwelling in water-rich conditions (see Section 5.2). However, more experiments and observations are needed to confirm these controversial implications.

Karato (1992) attributed seismological observations of weak anisotropy below 200 km depth (e.g., Beghein et al., 2006; Montagner and Anderson, 1989b; Montagner and Kennett, 1996) to deformation due to diffusion creep, which produces little or no LPO (Karato, 1988). However, Couvy et al. (2004) suggested that dislocation creep is still dominant in the deep upper mantle (below 300 km) with high-pressure experiments, and that below 330 km depth the slip direction of olivine changes to a different slip system, [001](hk0), with weak radial anisotropy (Mainprice et al., 2005). Karato et al. (2008) questioned Couvy et al.'s work because the exact values of stress at which LPO develops are unknown and the sample contains a significant amount of water, concluding that their results are consistent with C-type regime. On the other hand, Miyazaki et al. (2013) recently reported that olivine crystals can be aligned during diffusion creep, attributing weak anisotropy in the deep upper mantle to the weak E-type fabric developed in diffusion creep.

Other dominant minerals in the upper mantle, orthopyroxene and clinopyroxene are also anisotropic. Maximum V_S anisotropy for a single crystal of orthopyroxene is between 11.0% (Weidner et al., 1978) and 15.1% (Webb and Jackson, 1993), and clinopyroxene has V_S anisotropy between 20% and 24% (Collins and Brown, 1998; Levien et al., 1979). Seismically detectable LPO by large-scale deformation may be different in amplitude from LPO in a single crystal measured in laboratories.

High attenuation and low velocity in the asthenosphere have been initially attributed to partial melting in the 1970s (e.g., Anderson and Spetzler, 1970). Holtzman et al. (2003) provided an experimental basis for explaining the formation of melt segregation in sheared conditions. More recently, Kawakatsu et al. (2009) further supported the idea of partial melting in the asthenosphere by imaging a sharp lithosphere–asthenosphere boundary with receiver functions from ocean bottom seismometers in the Pacific. Thin layers of partial melt in the asthenosphere may cause strong radial anisotropy via SPO, with faster *SH* velocity than *SV* velocity. This is consistent with seismic observations in the central Pacific (e.g., Cara and Lévêque, 1988; Ekström and Dziewoński, 1998; Gung et al., 2003; Montagner and Tanimoto, 1991; see Section 5.1). Alternatively, the sub-solidus model, which attributes the characteristics of the asthenosphere to grain size or water content without invoking partial melting, might explain radial anisotropy in the asthenosphere. Readers may refer to Karato (2012) for details about the sub-solidus model.

3.2. Transition zone

Olivine transforms to wadsleyite at around 410 km depth, and wadsleyite transforms to ringwoodite at about 520 km depth. These minerals have different anisotropic properties. Wadsleyite may be the main source for anisotropy in the mantle transition zone, since other dominant minerals, ringwoodite and majoritic garnet, are weakly anisotropic (Mainprice et al., 2000). Zha et al. (1997) reported single crystal V_S anisotropy of 18% for Mg_2SiO_4 wadsleyite at ambient conditions, slightly decreasing to 13–14% at the pressure corresponding to 410 km depth. Tommasi et al. (2004) used forward models of LPO development in response to a given flow process to predict anisotropy produced by wadsleyite. They showed that V_{SH} is higher in horizontal shear, and V_{SV} is higher in vertical shear. Recently, Kawazoe et al. (2013) found experimentally that the dominant slip direction of wadsleyite is [001](010) for a water content of 50–230 wt. ppm H_2O. In this system, horizontal flow causes faster *SV* velocity, whereas vertical flow produces faster *SH* velocity.

Table 1
Dominant slip systems and radial anisotropy of olivine fabrics.

Fabric	Slip system	Horizontal flow	Vertical flow
A-type	[100](010)	$V_{SH}/V_{SV} > 1$	$V_{SH}/V_{SV} < 1$
B-type	[001](010)	$V_{SH}/V_{SV} > 1$	$V_{SH}/V_{SV} > 1$ (weak)
C-type	[001](100)	$V_{SH}/V_{SV} < 1$	$V_{SH}/V_{SV} > 1$ (weak)
D-type	[100]{0kl}	$V_{SH}/V_{SV} > 1$	$V_{SH}/V_{SV} < 1$
E-type	[100](001)	$V_{SH}/V_{SV} > 1$ (weak)	$V_{SH}/V_{SV} < 1$

Weidner et al. (1984) measured the elastic constants of Mg_2SiO_4 ringwoodite at ambient conditions to find a V_S anisotropy of 7.9%, and Mainprice et al. (2000) reported that it is nearly perfectly isotropic at transition zone pressures. Hence, anisotropy below 520 km depth may indicate SPO such as, for example, in laminated structures of oceanic crust and spinel-rich assembly in subducting slabs (Karato, 1997). Radial anisotropy in the mantle transition zone is poorly constrained seismically, as demonstrated by the significant differences between 1-D profiles of Montagner and Kennett (1996) and Visser et al. (2008) in Fig. 2, where other anisotropic models are also shown.

3.3. Lower mantle

The lower mantle consists mainly of (Mg,Fe,Al)(Si,Al)O_3 perovskite and (Mg,Fe)O ferropericlase. V_S anisotropy of $MgSiO_3$ perovskite is 33% at ambient conditions (Yeganeh-Haeri, 1994), but it varies to 8% at 1000 km depth and 13% at 2500 km depth when using the extrapolated temperature and pressure derivatives of Wentzcovitch et al. (2004). Li et al. (2006) showed that $CaSiO_3$ perovskite is nearly isotropic at lower mantle conditions. Karki et al. (1997) first estimated the anisotropy of MgO at high pressures corresponding to the lower mantle, predicting an increase of V_S anisotropy with increasing depth up to over 50% in the D″ region. Marquardt et al. (2009) reported that (Mg, Fe)O ferropericlase is almost isotropic near 660 km depth, and that its V_S anisotropy increases considerably with increasing pressure (depth). Maximum V_S anisotropy of (Mg,Fe)O reaches up to 40% in the D″ region. Anisotropy is further enhanced in (Mg,Fe)O with increasing iron content.

At the base of the lower mantle (D″ region), Hirose et al. (1999) argued that former oceanic crust would be partially molten if temperatures were larger than 4000 K. Kendall and Silver (1996, 1998) also supported the idea of partial melting in subducting slabs at the lowermost mantle based on strong radial anisotropy measured with core-reflecting phases. This melt could form detectable SPO, although the presence of partial melting in subducting slabs is questionable due to their low temperatures and observed high seismic velocities.

The discovery of the perovskite to post-perovskite transition at the base of the lower mantle (Murakami et al., 2004; Oganov and Ono, 2004) brought new ideas into the debate on the origin of D″ anisotropy. There are several proposals for slip systems of post-perovskite (Mao et al., 2010; Merkel et al., 2006, 2007; Miyagi et al., 2010; Yamazaki et al., 2006), but consensus has not been reached yet. The slip system proposed by Miyagi et al. (2010) produces faster *SH* and *SV* velocity associated with horizontal and vertical flow, respectively, which reconciles D″ seismic observations with geodynamical implications. For example, faster *SH* velocity has been observed beneath circum-Pacific regions, where ancient slabs may have reached the core–mantle boundary (CMB), causing horizontal flow (e.g., Kendall and Silver, 1996; Lay and Helmberger, 1983; Lay and Young, 1991; Ritsema, 2000). Wenk et al. (2011) performed geodynamic simulations to test various slip systems of post-perovskite and found that post-perovskite with dominant (001) slip system (Miyagi et al., 2010) is consistent with observed radial anisotropy. However, their experiments had some limitations; e.g., a 2-D scheme assuming infinite frequency seismic wave propagation was used, and pure Mg–Si–O phases were considered neglecting compositional heterogeneity.

If temperature is high near the CMB, $MgSiO_3$ perovskite is more stable than post-perovskite, and potentially more influential on anisotropy in D″. Karato et al. (1995) used $CaTiO_3$ as an analogue material of $MgSiO_3$ to perform deformation experiments. Mainprice et al. (2008) calculated the dislocation glide in Mg-perovskite at lower mantle pressure and 0 K temperature conditions. Using the elastic constants of Oganov et al. (2001) for temperature of 1500 K and 3500 K and pressures of 38 GPa and 88 GPa, they inferred seismic anisotropy of

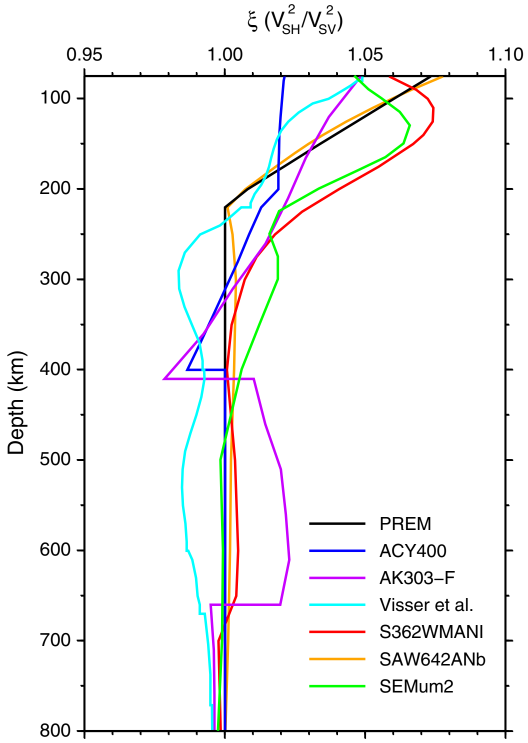

Fig. 2. Comparison of 1-D radial anisotropic models from PREM (Dziewoński and Anderson, 1981), ACY400 (Montagner and Anderson, 1989b), and AK303-F (Montagner and Kennett, 1996) with average profiles from 3-D anisotropic models from S362WMANI (Kustowski et al., 2008), SAW642ANb (Panning et al., 2010), and SEMum2 (French et al., 2013).

Mg-perovskite, where the faster *SV* velocity observed in D″ (e.g., Kawai and Geller, 2010; Panning and Romanowicz, 2004; Pulliam and Sen, 1998; Russell et al., 1998) would be caused by horizontal flow. However, there are no experimental results yet on the deformation of perovskite under high pressure and temperature conditions to make a solid connection between seismic observations and mineral physics experiments. Furthermore, faster *SH* velocity also has been observed beneath the Pacific (e.g., Fouch et al., 2001; Ritsema et al., 1998; Vinnik et al., 1995, 1998), which makes it difficult to interpret the radial anisotropy in the LLSVPs.

Ferropericlase can also play a significant role in anisotropy in D″ in spite of its small volume abundance (~20 vol.%) in the lower mantle. Karato (1998a,b) first pointed out LPO of MgO as a likely mechanism to cause D″ anisotropy. Marquardt et al. (2009) demonstrated that 20 vol.% of $(Mg_{0.8}Fe_{0.2})O$ contributes similarly as 80 vol.% $MgSiO_3$ to the overall anisotropy. Furthermore, Yamazaki and Karato (2002) reported that ferropericlase shows radial anisotropy of $V_{SH} > V_{SV}$ in horizontal shear, consistent with seismic observations. Therefore, ferropericlase could be a potential origin for the observed anisotropy in D″. Recently, tilted transverse isotropy has been interpreted in the D″ region beneath the Caribbean (e.g., Garnero et al., 2004; Maupin et al., 2005; Nowacki et al., 2010), which suggests that symmetry systems more complex than hexagonal symmetry may be needed to better understand D″ radial anisotropy. Karato (1998b) also claimed the possibility of the tilting of melt pockets in D″.

4. Previous global studies of radial anisotropy

Several global studies have investigated radial anisotropy as a function of the Earth's radius. As mentioned previously, the global 1-D reference Earth model PREM includes an anisotropic zone, with radial anisotropy monotonously decreasing with depth from a value of $\xi =$ 1.10 ($\xi = \frac{V_{SH}^2}{V_{SV}^2}$) at the Moho (24.4 km) to $\xi = 1.0$ at 220 km depth (see Fig. 2).

Montagner and Anderson (1989b) used additional normal mode data that had accumulated since 1981 as well as the data used in the construction of PREM, obtaining the ACY400 model, which has around 1.02 of radial anisotropy down to 200 km depth and negative anisotropy (down to $\xi = 0.987$) in the 300–400 km depth range (see Fig. 2). Montagner and Kennett (1996) extended observations of radial anisotropy down to the uppermost lower mantle (~1000 km depth) by using both body wave and normal mode data and including anelasticity, density, and three anisotropic parameters, ξ, ϕ, and η, in the inversion (see model AK303-F in Fig. 2). They found positive anisotropy in the transition zone bounded by a quite distinct negative anisotropy signal immediately above and below this region.

Beghein et al. (2006) reported that radial anisotropy is negligible in the transition zone when applying an inverse probabilistic approach to normal mode and surface wave phase velocity data. Visser et al. (2008) used a new dataset of fundamental and higher-mode phase velocity data to infer the presence of negative anisotropy ($V_{SV} > V_{SH}$) in the transition zone, in disagreement with the results of Montagner and Kennett (1996). These discrepancies between spherically averaged radial anisotropy models highlight the difficulties in constraining radial anisotropy robustly even in the form of 1-D depth profiles (see Fig. 2).

Nataf et al. (1984, 1986) built the first models of 3-D radial anisotropy in the upper mantle expanded in spherical harmonics up to degree 6 based on long-period (100–330 s) fundamental-mode surface wave data. These pioneering studies were followed by the work of Montagner and Tanimoto (1991), who inverted long-period (70–250 s) surface waves to image azimuthal and radial anisotropy simultaneously. Shapiro and Ritzwoller (2002) employed a Monte-Carlo technique to constrain radial anisotropy in the upper mantle using fundamental-mode surface-wave phase and group velocity data. In addition, higher-mode surface waves were utilized to constrain radial anisotropy in the deeper mantle (e.g., Debayle and Kennett, 2000; Gung et al., 2003).

Finally, whole mantle radial anisotropy models were constructed by Panning and Romanowicz (2006), Kustowski et al.(2008), and Panning et al. (2010). These models were built with different datasets, model parameterizations, and sensitivity kernels. Kustowski et al. (2008) adopted sensitivity kernels calculated using classical ray theory to model surface wave phase anomalies with a period range of 35 to 150 s, long-period waveforms (body waveforms with $T > 50$ s and mantle waveforms with $T > 125$ s), and body wave travel times. Panning et al. (2010) utilized NACT to build 2-D sensitivity kernels and invert long-period body waveforms ($T > 32$ s) and surface waveforms ($T > 60$ s). Recently, French et al. (2013), following Lekić and Romanowicz (2011), built a new upper mantle model of radial anisotropy. They applied a more accurate 3-D forward modeling scheme based on the spectral element method (Capdeville et al., 2003) combined with NACT sensitivity kernels to model long-period waveforms ($T > 60$ s). These three models (French et al., 2013; Kustowski et al., 2008; Panning et al., 2010) are extensively compared in Section 6.

5. Characteristic features of radial anisotropy at the regional scale

There are a few regions where observations of radial anisotropy have been reported and confirmed by various researchers, thereby suggesting that they are robust and reproducible. In this section, we review key findings from regional studies, which will play an important role when discussing 3-D global models of whole mantle radial anisotropy in Section 6.

5.1. Central Pacific

Oceanic lithosphere undergoes a relatively simple horizontal movement from ridge to trenches, unlike continental lithosphere that

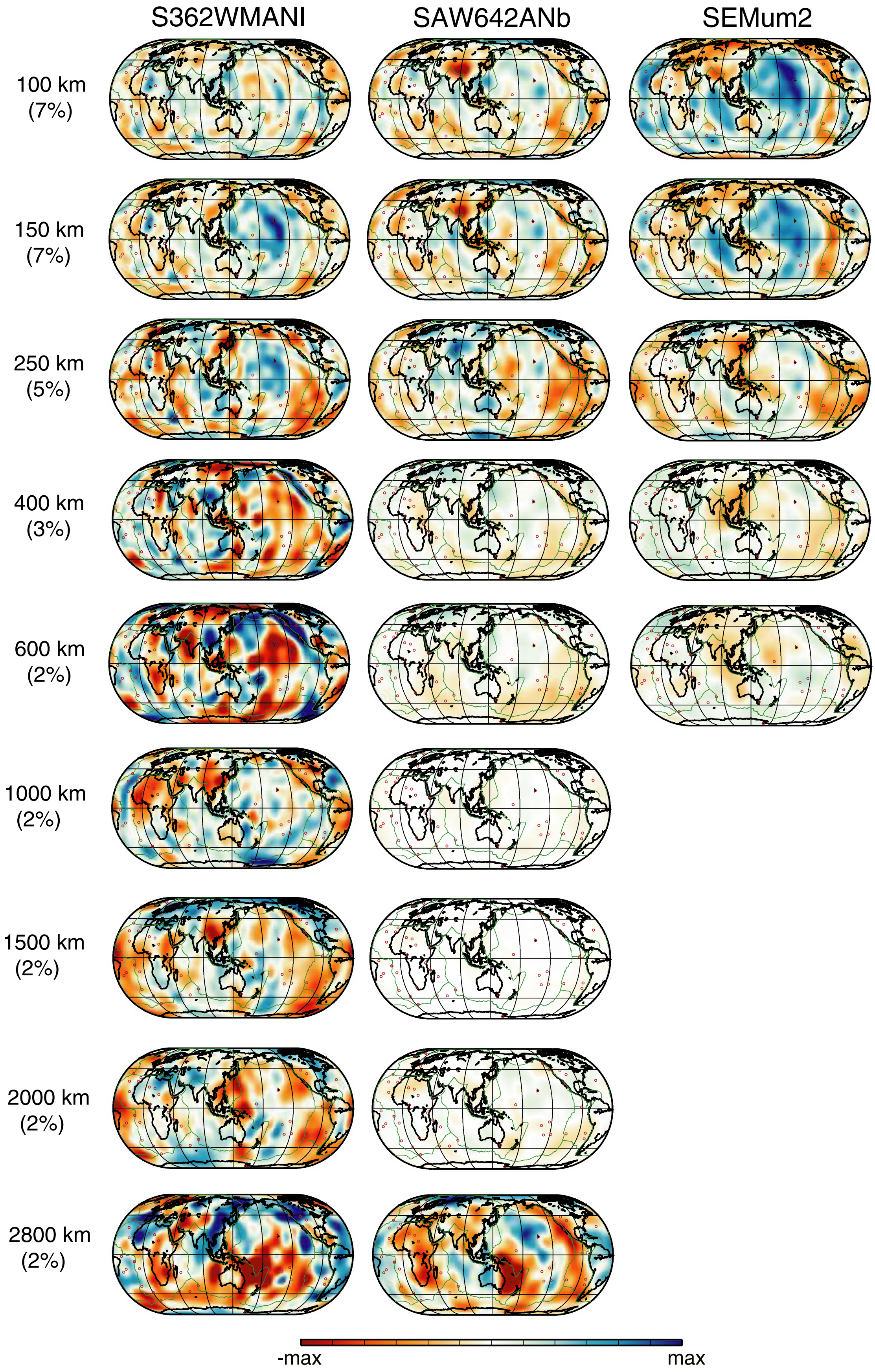

Fig. 3. Comparison of radial anisotropy from S362WMANI (Kustowski et al., 2008), SAW642ANb (Panning et al., 2010), and SEMum2 (French et al., 2013) at depths of 100, 150, 250, 400, 600, 1000, 1400, 2000, and 2800 km. Perturbation scale at each depth is shown below depths. The perturbations are estimated with respect to PREM, and average values are subtracted from each depth slice. Hotspots are indicated in red circles, and plate boundaries are depicted in green lines.

remains for a longer time above the asthenosphere. The oceanic lithosphere and asthenosphere beneath the Pacific may experience the largest horizontal deformation due to the fast sea floor spreading along the East Pacific Rise, resulting in strong olivine LPO. Cara and Lévêque (1988) and Montagner and Tanimoto (1991) measured substantial radial anisotropy ($\xi \sim 1.05$) beneath the Pacific using surface wave data. Ekström and Dziewoński (1998) confirmed the strong positive radial anisotropy ($V_{SH} > V_{SV}$) with respect to PREM beneath the central Pacific with a complex distribution not directly correlated to the age of the sea floor. This is also found in the 3-D whole mantle model of radial anisotropy by Gung et al. (2003) and Kustowski et al. (2008).

Karato (2008) attributed the significant radial anisotropy ($V_{SH} > V_{SV}$) and weak azimuthal anisotropy beneath Hawaii, high viscosity, and low electrical conductivity to a lower water content due to removal of water from the plume after partial melting, which results in A-type olivine LPO surrounded by E-type olivine LPO in ambient asthenosphere. Mantle convection simulations by Becker et al. (2008) that take into account lateral variations in viscosity and LPO formation, mimic the radial anisotropy model beneath the Pacific obtained by Kustowski et al. (2008). They attributed the anisotropy beneath the central Pacific to shearing in the asthenosphere, but LPO may saturate at strains much lower than the strains required for Becker et al.'s calculations (Karato, 2008).

5.2. East Pacific Rise

The East Pacific Rise has the highest sea floor spreading rate among ridges. Hence, it is a source of strong radial anisotropy. Two directions of flows are expected here: vertical flow at deep depth beneath the ridge to feed the generation of new oceanic crusts and horizontal flow at shallow depth to transfer them to trenches over the Pacific.

Nishimura and Forsyth (1989) observed an age dependence of radial anisotropy beneath the Pacific from the inversion of fundamental-mode Rayleigh-wave ($T = 20–125$ s) and Love-wave ($T = 33–125$ s) phase-velocity data. They proposed the transition of mantle flow beneath the East Pacific Rise by interpreting small radial anisotropy observed in the youngest region (0–4 Ma) of the Pacific as a mixing of vertical and horizontal mantle flows. Webb and Forsyth (1998) found $V_{SH} > V_{SV}$ down to 100 km depth using data from ocean bottom seismometers deployed along the East Pacific Rise. Wolfe and Solomon (1998) argued that large values (~2 s) of shear-wave splitting off the East Pacific Rise are due to the combined effects of spreading-induced flow above a depth of 100 km with the vertical return flow from the upper mantle to the ridge axis. Global tomographic models (e.g., Gung et al., 2003; Kustowski et al., 2008; Montagner and Tanimoto, 1991) also show the transition of radial anisotropy beneath the East Pacific Rise. Gu et al. (2005) confirmed the transition from a vertical mantle flow at greater depths (200–300 km) to a horizontal flow at shallower depths beneath the East Pacific Rise by inverting a large set of seismic waveforms, body-wave travel times, and phase velocity measurements.

5.3. Lithosphere–asthenosphere boundary

The boundary between the lithosphere and asthenosphere might be the locus for abrupt changes in radial anisotropy, since anisotropy in the lithosphere is thought to be related to past strain field (frozen-in anisotropy; Silver, 1996), whereas anisotropy in the asthenosphere is likely related to present mantle flow (Montagner, 1998). This characteristic of anisotropy may be useful to detect the depth extent of continental roots. Following reports by Montagner and Tanimoto (1991) and Montagner (1998), Gung et al. (2003) confirmed the presence of faster *SH* velocity at the bottom of continental and oceanic lithosphere using waveform data. Due to different thicknesses of continental and oceanic lithospheres, faster *SH* velocity is observed at 80–250 km depth beneath oceanic lithosphere, and at 250–400 km depth beneath continental lithosphere.

5.4. D″ region

As discussed in Section 3.3, the bulk of the lower mantle appears to be isotropic except in the D″ region. Faster *SH* velocity is observed in D″ beneath the circum-Pacific regions where subducting slabs reach the CMB (e.g., Kendall and Silver, 1996; Lay and Helmberger, 1983; Lay and Young, 1991; Ritsema, 2000), while faster *SV* and *SH* velocities are mixed in the two large low shear-velocity provinces (LLSVPs) beneath the South Pacific and Africa (e.g., Fouch et al., 2001; Kawai and Geller, 2010; Kendall and Silver, 1996; Kustowski et al., 2008; Panning and Romanowicz, 2004, 2006; Panning et al., 2010; Pulliam and Sen, 1998; Ritsema et al., 1998; Russell et al., 1998; Vinnik et al., 1995, 1998). These features of anisotropy may imply mantle convection in the lowermost mantle such as horizontal movements beneath subduction zones and vertical flows in the two LLSVPs if simplified.

However, this interpretation hinges on many assumptions, notably on the slip systems of post-perovskite in the D″, which are still under

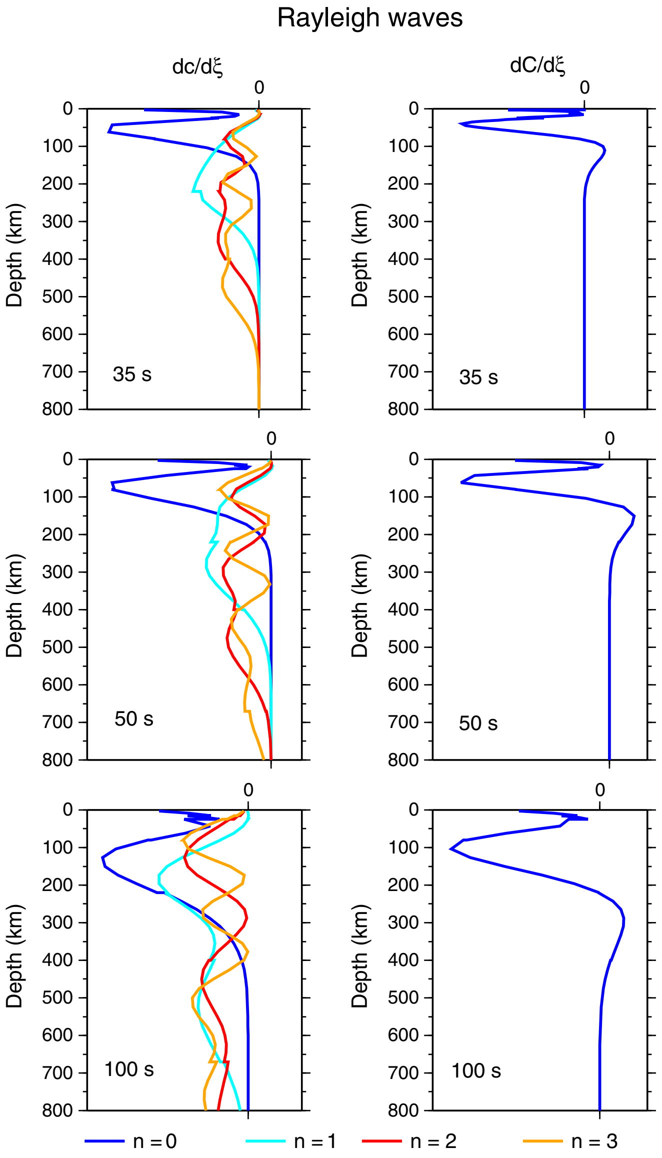

Fig. 4. Sensitivity kernels of Rayleigh-wave phase and group velocities with respect to radial anisotropy. (Left) Phase velocity kernel with respect to radial anisotropy. Sensitivity kernels at periods of 35, 50 and 100 s are presented from top to bottom. The kernel for fundamental mode is depicted in blue, and the kernels of overtones up to number 3 are indicated in cyan, red, and orange colors. (Right) Group velocity kernel with respect to radial anisotropy. The details are the same as in the left column.

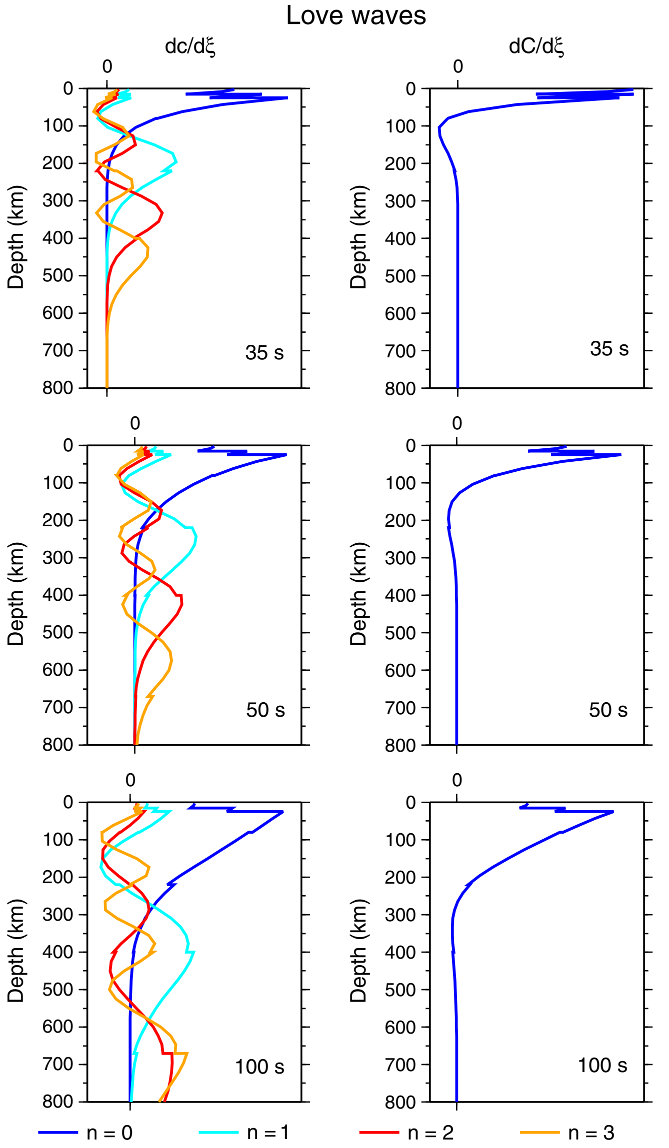

Fig. 5. Sensitivity kernels of Love-wave phase and group velocities with respect to radial anisotropy. (Left) Phase velocity kernel with respect to radial anisotropy. The kernel for fundamental mode is depicted in blue, and the kernels of overtones up to number 3 are indicated in cyan, red, and orange colors. (Right) Group velocity kernel with respect to radial anisotropy. The details are the same as in the left column.

debate (e.g., Mao et al., 2010; Merkel et al., 2006, 2007; Miyagi et al., 2010; Yamazaki et al., 2006). Perovskite and Ferropericlase may also play a role in the development of radial anisotropy in the D″ region as discussed in Section 3.3. Readers are referred to review articles such as by Kendall and Silver (1998), Kendall (2000), Wookey and Kendall (2007), Yamazaki and Karato (2007), and Nowacki et al. (2011) for further details about anisotropy in D″.

6. Comparisons of whole-mantle radially anisotropic models

In this section, we compare the most recent 3-D whole-mantle radially anisotropic models, SAW362ANb (Panning et al., 2010), S362WMANI (Kustowski et al., 2008), and SEMum2 (French et al., 2013). Although SEMum2 only covers the upper mantle, it is interesting to compare it with the other two whole-mantle models, since it was built with an improved 3-D forward modeling scheme. Perturbations in radial anisotropy of the three models from the average values are presented in Fig. 3.

In all models the amplitude of the anomalies in radial anisotropy decreases with increasing depth except within the D″ region, where the strength of the anomalies increases, notably for the model SAW642ANb. While there are common features between the models, overall there are more discrepancies among the models than similarities. For example, the faster *SH* velocity at 150–250 km depth beneath the central Pacific, which was discussed in Section 5.1, appears clearly in S362WMANI and SEMum2, but is hardly visible in SAW642ANb. A polarity change of radial anisotropy beneath the East Pacific Rise (from $V_{SH} > V_{SV}$ at 100 km depth to $V_{SH} < V_{SV}$ at 200–300 km depth; see Section 5.2) is observed in S362WMANI. On the other hand, faster *SV* velocity persists in SAW642ANb and SEMum2 in the 100–300 km depth range, with no change in the polarity of radial anisotropy being observed.

On the contrary, faster *SH* velocity beneath the continents at around 250 km is clear in S362WMANI and SAW642ANb, probably related to the depth of the lithosphere–asthenosphere boundary (LAB; Gung et al., 2003), but SEMum2 shows only faster *SV* velocity beneath almost all continental lithosphere down to 600 km depth. In the D″ region, S362WMANI and SAW642ANb depict faster *SV* velocity in the two LLSVPs beneath the southern Pacific and Africa. However, there are also significant differences; in S362WMANI, the pattern of faster *SH* velocity follows the boundaries of the western Pacific and Alaska, whereas in SAW642ANb, faster *SV* velocity is observed beneath the East Pacific Rise and China.

In conclusion, S362WMANI seems to be most consistent with the regional studies discussed in Section 5, but it shows strong anisotropy

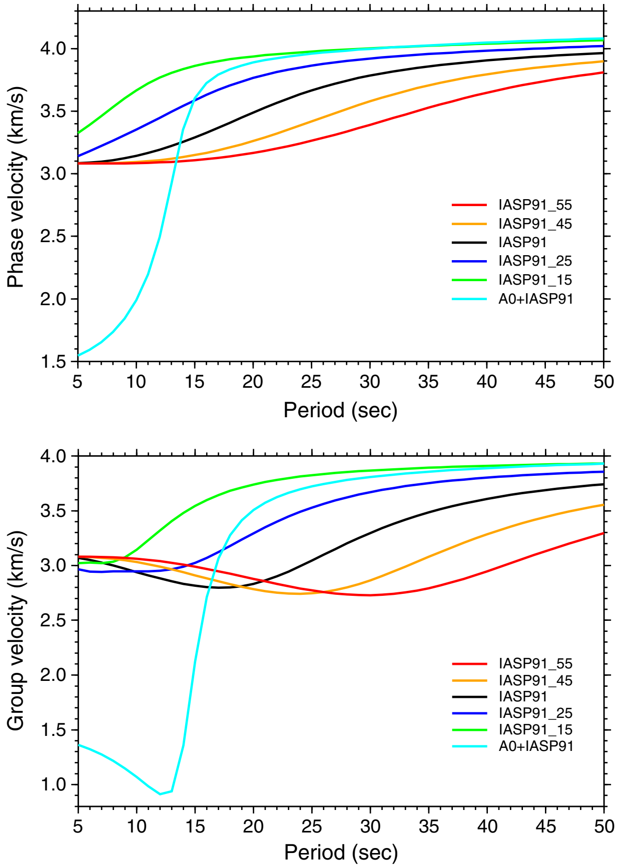

Fig. 6. Phase and group velocity dispersion curves for various tectonic settings with different Moho depths. (Top) Phase velocity dispersion curve for a period range of 5 to 50 s. IASP91 (Kennett and Engdahl, 1991) is modified to have different Moho depths, which is shown as suffix to IASP91. For example, IASP91_55 means IASP91 with Moho depth of 55 km. A0 + IASP91 means the combination of A0 in CRUST2.0 (Bassin et al., 2000) that is typical oceanic crust and IASP91 for mantle structure. (Bottom) Group velocity dispersion curve for a period range of 5 to 50 s. The same models as in phase velocity dispersion curves are used to build dispersion curves.

(~2%) in the whole lower mantle, which may be inconsistent with the relatively isotropic behavior of perovskite and ferropericlase in the upper part of the lower mantle, as mentioned in Section 3.3.

7. Sensitivity kernels and synthetic tests

Different data types have distinct depth resolutions and complementary sensitivities to the Earth's deep anisotropic structure. In this section, we discuss the sensitivity and resolution of various datasets to radial anisotropy, notably of: (i) fundamental-mode surface-wave phase- and group-velocity data; (ii) higher-mode phase-velocity measurements; and (iii) body-wave travel times.

7.1. Surface-wave sensitivity kernels

Surface waves are very useful to study radial anisotropy globally because of their nearly constant along-path sensitivity to Earth structure. With good source–receiver coverage, they enable a better sampling of the upper mantle and transition zone than body waves. While fundamental and higher-mode surface-wave phase-velocity data are key to image the Earth's upper mantle and transition zone, respectively, surface-wave group-velocity data provide useful constraints on crustal structure. Figs. 4 and 5 show sensitivity kernels of Rayleigh and Love waves calculated using the great-circle approximation (e.g., Woodhouse and Dziewoński, 1984), for the PREM model. The kernels are the partial derivatives of phase velocity (left columns) and of group velocity (right columns) with respect to $\delta\xi$ for various wave periods and overtone numbers. In the left column of Fig. 4, the probing depth increases with increasing overtone number. As expected, shorter-period surface waves are sensitive to shallower structure than longer-period data. In the right column, the fundamental-mode group-velocity kernels shown for various wave periods highlight that group-velocity data probe shallower depths than corresponding phase velocities with the same wave periods (shown in the left column). Therefore, group-velocity data are more suitable to estimate shallow structure, notably crustal structure, than phase-velocity data.

Fig. 5 shows that Love-wave sensitivity kernels have a similar behavior to Rayleigh-wave kernels as a function of wave period and overtone number. Fundamental-mode Love-wave sensitivity kernels for long periods have different shape of depth sensitivity from corresponding Rayleigh-wave kernels with the same periods. In order to investigate radial anisotropy in a broad depth range with uniform coverage, it is important to combine fundamental mode, overtone, and phase/group-velocity surface-wave data with a wide period range.

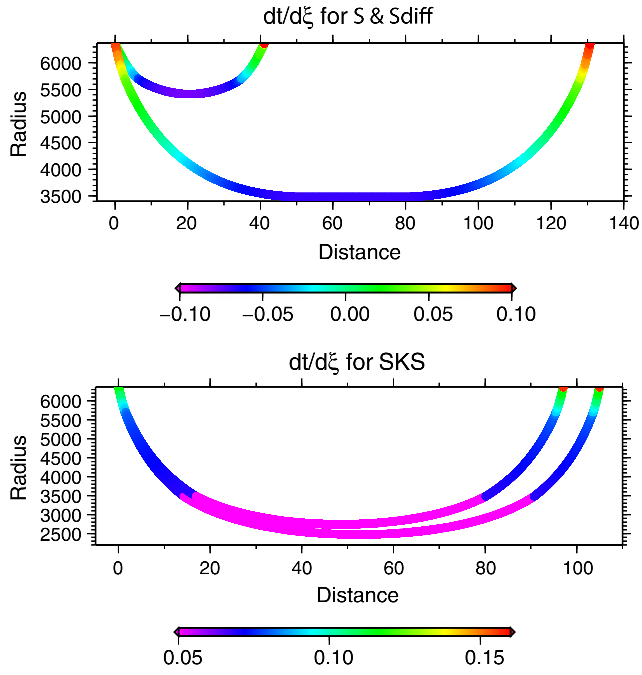

Fig. 7. Sensitivity kernels of travel times with respect to radial anisotropy. (Top) Sensitivity kernels for S and Sdiff phases. (Bottom) Sensitivity kernel for SKS phase.

7.2. Sensitivity to Moho depth

In addition to velocity structure, surface waves are also sensitive to Moho depth variations. Fig. 6 shows illustrative examples of theoretical phase- and group-velocity dispersion curves for various Moho depths (from 15 km to 55 km), including an example for typical oceanic crust. As the Moho depth increases, the phase and group velocities at longer periods decrease due to the increasing influence of the crust. In particular, the group-velocity dispersion curves show wider period ranges of low velocities called the Airy phase.

Lebedev et al. (2013) investigated the sensitivity of phase and group velocities with respect to Moho depth, and found that Rayleigh waves are more sensitive to perturbations in Moho depth than Love waves. For example, a change in Moho depth of 1 km causes a perturbation in Rayleigh-wave group velocity of 1%, while a Moho depth variation of 2 km is needed for the same perturbation of Love-wave group velocity. Moreover, they also highlighted that group-velocity data are better suited than phase velocity to constrain Moho depth. The use of short-period group-velocity data in the context of radially anisotropic tomography will be discussed below in Section 8.1.

7.3. Sensitivity kernels of body-wave travel times

Body-wave travel times constrain lower mantle structure, including radial anisotropy. Direct phases such as *S*, *SS*, and *SSS*, core-reflecting phases such as *ScS*, *ScS2*, and *ScS3*, and depth phases such as *sS* are measured on transverse component seismograms to avoid being obscured by *P*-type waves. They are sensitive to horizontally polarized perturbations of seismic velocity (V_{SH}) when rays are traveling quasi-horizontally, notably near the turning point. Conversely, they are sensitive to vertically polarized perturbations (V_{SV}) for quasi-vertically traveling rays. Fig. 7 shows illustrative examples of sensitivity kernels of *S*, *Sdiff*, and *SKS* wave travel times with respect to $\delta\xi$ for the PREM Earth model calculated using the formalism of Woodhouse (1981) and Woodhouse and Girnius (1982). The kernels for *S* and *Sdiff* have positive values at depths shallower than about 400 and 1900 km depths in this example, respectively. Therefore, if positive radial anisotropy ($V_{SH} > V_{SV}$) exists at such shallower depths, it increases the travel times (see Eq. (11)). On the other hand, negative radial anisotropy ($V_{SV} > V_{SH}$) at shallower depths decreases the travel times. For deeper depths, the kernels for these phases have negative values (see Fig. 7). Hence, the presence of positive radial anisotropy in the deep mantle, decreases the travel times of transverse-component body waves.

Phases such as *SKS*, *SKKS*, and *sSKS* are measured on the vertical or longitudinal components, since these phases are vertically polarized after leaving the core, where the waves travel as *P* phases. These phases are sensitive to vertically polarized perturbations of seismic velocity regardless of traveling angle and depth. Fig. 7 shows that their sensitivity kernels have positive values for the whole ray path, which means that positive radial anisotropy always increases travel times.

7.4. Model resolution tests for surface-wave and body-wave data

As discussed in Section 4, several datasets are usually combined to image global mantle structure. In order to assess the reliability of tomographic inversions and the resolving power of the various datasets, checkerboard tests are often performed. Synthetic data are calculated for a given input model with an alternating pattern using the same source–receiver pairs as in the real data. The synthetic data are then

(a) Checkerboard tests for anisotropic structure

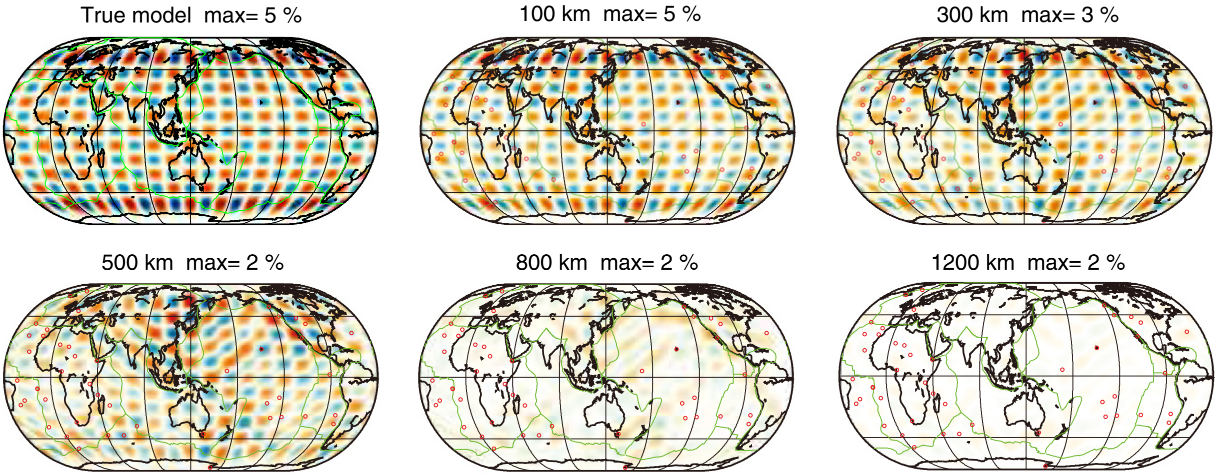

(b) Checkerboard tests for isotropic structure

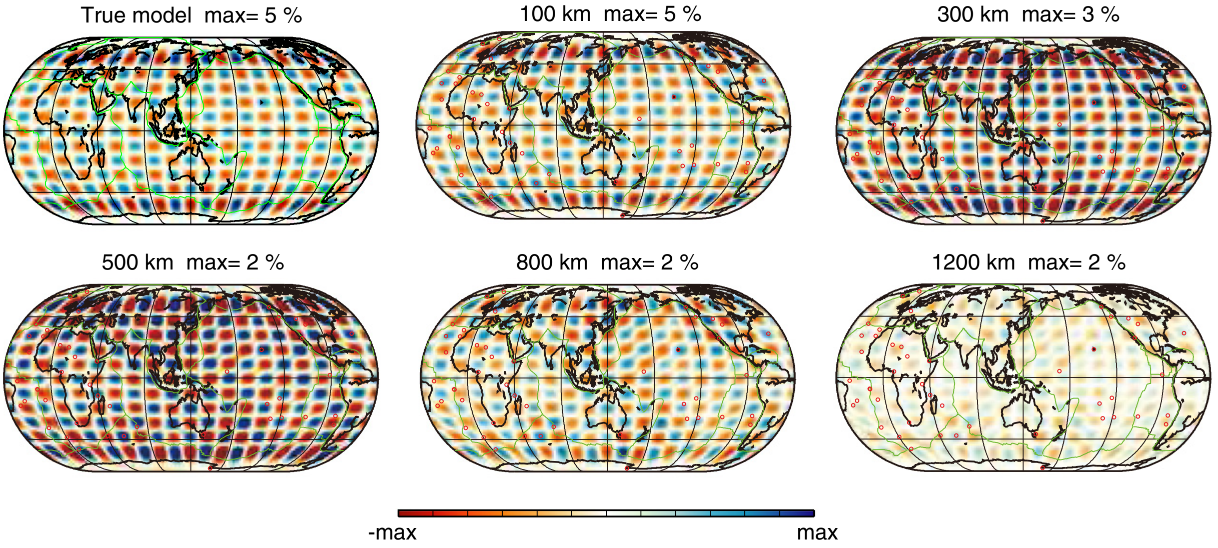

Fig. 8. Checkerboard tests with surface wave data used in the construction of S40RTS (Ritsema et al., 2011) with addition of Love-wave phase velocity data and group velocity data (Ritzwoller and Levshin, 1998). The true model is shown on the top left side, and depth slices are shown for 100, 300, 500, 800, and 1200 km depths. (a) Test results for the anisotropic models. (b) Results for the isotropic models.

inverted to verify how well the input model is recovered. Figs. 8 and 9 show the results of checkerboard tests designed to investigate the resolving power of body and surface wave data in global inversions for radially anisotropic structure.

First, we examine the resolving power of surface-wave data by considering a set of input checkerboards with 2000 km width. We use the same Rayleigh wave ray paths as used in the construction of S40RTS (Ritsema et al., 2011). Moreover, we also include Love wave source–receiver paths as in the set of Love wave measurements produced by the same authors and group velocity data by Ritzwoller and Levshin (1998). Fig. 8 shows that surface waves have a good resolving power for anisotropic structure in the upper mantle and in the mantle transition zone, and a limited resolution for the lower mantle. The corresponding checkerboard tests for travel times with the same ray paths as in the S40RTS body-wave dataset are presented in Fig. 9. They show fair to good resolution for radial anisotropy parameters in the lower mantle, but very limited resolution in the upper mantle. As expected, Figs. 8 and 9 show that isotropic structure is better resolved than anisotropic structure in both surface-wave and body-wave inversions. While these resolution tests indicate that the excellent data coverage of the multiple data sets used helps resolving radial anisotropy in the whole mantle, it is worth noting that checkerboard tests have their own limitations. For example, they do not test the impact of approximations in the underlying theory used to construct the models; future validation tests of the models using more sophisticated forward modeling tools should help us better understanding these issues. Overall, the results of checkerboard tests in Figs. 8 and 9 demonstrate that body and surface wave datasets are highly complementary (see also Ritsema et al., 2004) and thus it is important to combine both datasets to resolve radial anisotropy in the whole mantle.

8. Current challenges and new developments

As we discussed previously, there are large uncertainties in the models and there remains scope for progress in global anisotropy tomography. In this section, we discuss some factors hindering progress in global whole-mantle radial anisotropy imaging: the influence of the crust, trade-offs between isotropic and anisotropic structure, and limitations in methodology. In addition, we present a new global mantle model of radial anisotropy built to address some of these issues.

(a) Checkerboard tests for anisotropic structure

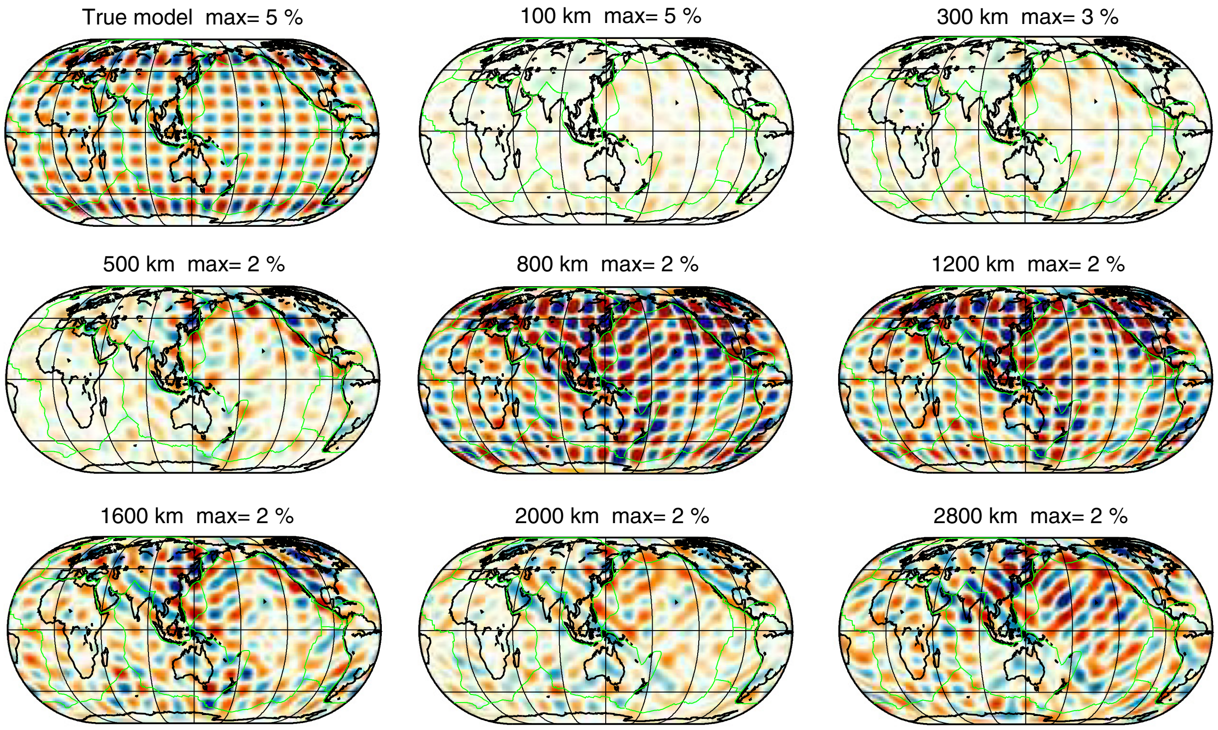

(b) Checkerboard tests for isotropic structure

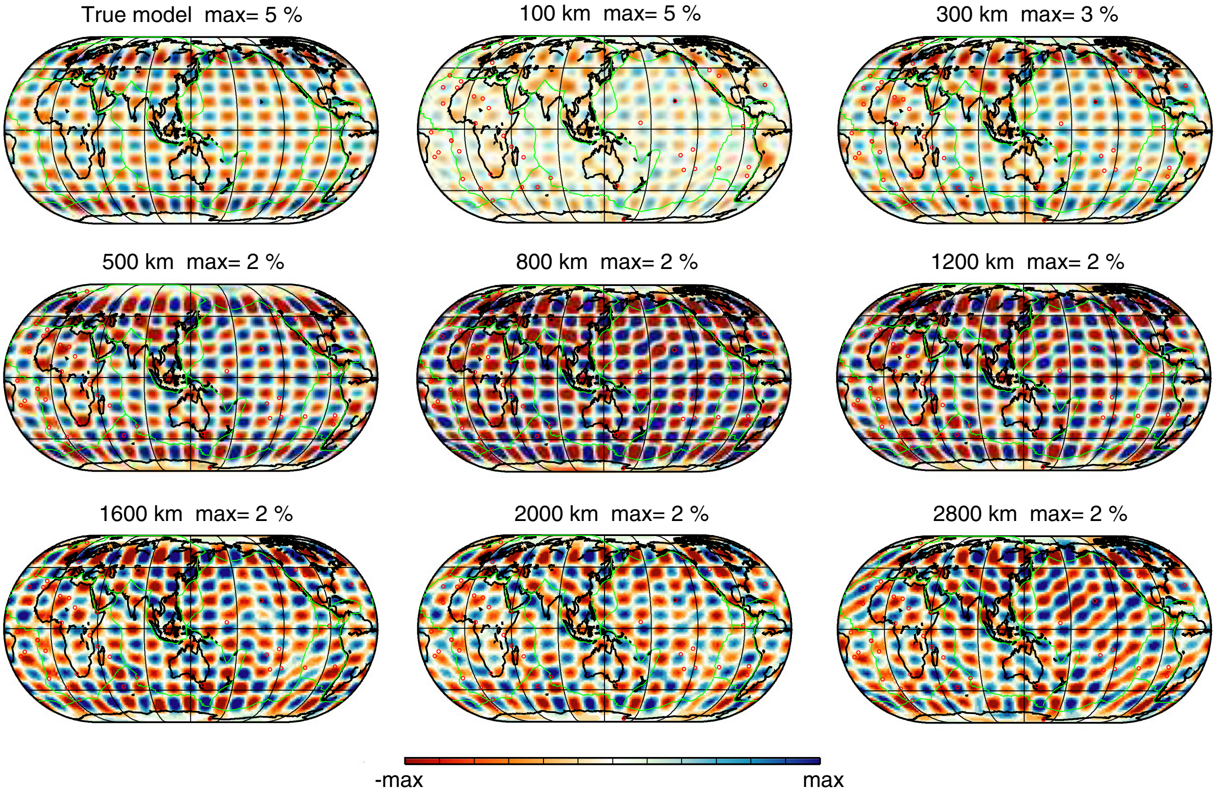

Fig. 9. Checkerboard tests for travel time data used in the construction of S40RTS (Ritsema et al., 2011). The true model is shown on the top left side and depth slices are shown for 100, 300, 500, 800, 1200, 1600, 2000, and 2800 km depth. (a) Test results for the anisotropic models. (b) Results for the anisotropic models.

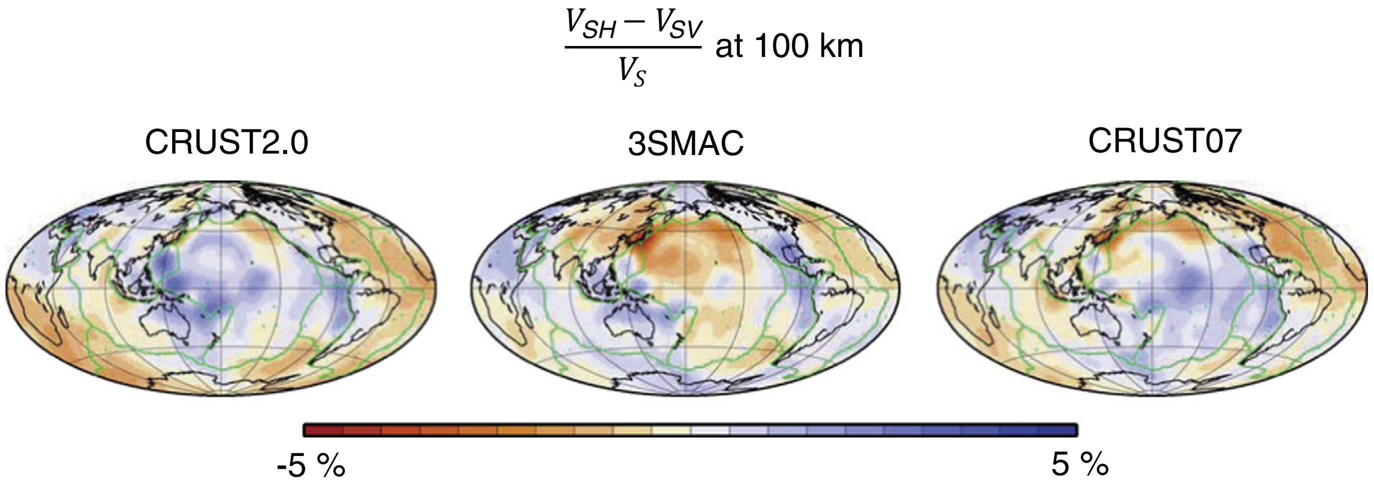

Fig. 10. Significant effect of crustal correction on radial anisotropy. Radial anisotropy at 100 km depth with different crustal correction using three crustal models, CRUST2.0 (Bassin et al., 2000), 3SMAC (Nataf and Ricard, 1996), and CRUST07 (Meier et al., 2007) are presented. This figure is modified from Ferreira et al. (2010).

8.1. The influence of the crust

The crust has a large effect on surface waves (e.g., Bozdağ and Trampert, 2008), so it is essential to remove the effects of the crust from surface wave data before performing inversions for mantle properties. Without proper crustal corrections, crustal structure can be mapped into the imaged mantle structure. If we knew the crustal structure perfectly well, it would be straightforward to determine crustal corrections based on "secondary" measurements (e.g., travel times, phase/group velocity data). In this case, crustal corrections can be estimated using, e.g., normal mode theory (e.g., Takeuchi and Saito, 1972). This approach has the advantage of considering rapid variations between continental and oceanic crust. Unfortunately, we do not know the structure of the crust in detail. The use of imperfect crustal models distorts mantle models. For example, Fig. 10 shows a map of perturbations in radial anisotropy at 100 km depth obtained using crustal corrections from three different existing crustal models – CRUST2.0 (Bassin et al., 2000), 3SMAC (Nataf and Ricard, 1996), and CRUST07 (Meier et al., 2007) – modified from Ferreira et al. (2010). The anisotropy model obtained using crustal corrections from CRUST2.0 is much different from the one with crustal corrections from 3SMAC, especially beneath the Pacific. If used for geodynamical interpretations, these models might lead to different implications in terms of mantle convection.

Fig. 11 compares the models of radial anisotropy SAW642AN (Panning and Romanowicz, 2006) and SAW642ANb (Panning et al., 2010). These two models are constructed with the exact same datasets, parameterization, and crustal model (CRUST2.0). However, different methods to determine crustal corrections are used. While SAW642AN is based on the non-linear crustal correction scheme of Marone and Romanowicz (2007), SAW642ANb is constructed using the 'modified linear correction' technique by Lekić et al. (2010), which mimics the non-linear crustal correction with enhanced computational efficiency. Fig. 11 shows that there are persistent discrepancies between the two models from 100 km to 600 km depth. A decreasing amplitude of radial anisotropy in this depth range in SAW642ANb is missing in SAW642AN. Even at a depth of 100 km, where the two models have similar amplitudes, the pattern of radial anisotropy beneath the Pacific is quite different.

The two examples clearly demonstrate the large influence of crustal corrections on imaged models of radial anisotropy. Current models of crustal structure are incomplete, and, in waveform tomography, accurate crustal correction modeling schemes are required to stabilize the nonlinear problem (e.g., Kustowski et al., 2007; Lekić et al., 2010; Marone and Romanowicz, 2007).

In Section 7.2, we pointed out that surface-wave group-velocity data are more sensitive to Moho depth than phase-velocity data. The relatively strong sensitivity of group velocity is also clear when comparing the crustal corrections for fundamental-mode phase and group velocity data shown in Figs. 12 and 13. Crustal corrections for group velocities are at least two times larger than those for phase velocities (note that the amplitude scale of group velocity perturbations in Fig. 13 is twice that for phase velocity in Fig. 12). Therefore, using group-velocity data with large sensitivity to crust in global radially anisotropic tomography could be a useful alternative to simple crustal corrections based on inaccurate crustal models.

8.2. New global radially anisotropic Earth model

Based on the experiments discussed in the previous sections, our strategy is to use a diverse dataset and to incorporate Moho perturbations to the inversions in order to address crustal effects consistently (Chang et al., 2012). We collected surface-wave phase-velocity data up to overtone number 6 from Ritsema et al. (2011) and group-velocity data from Ritzwoller and Levshin (1998). We use the same inversion scheme as in Ferreira et al. (2010), with body-wave travel times added to the modeling using the theoretical developments of Woodhouse (1981) and Woodhouse and Girnius (1982). The models are parameterized horizontally using spherical harmonic basis functions expanded up to degree 35, and 21 spline functions are used for variations in the radial direction (see Fig. 4 in Ritsema et al., 2004). Horizontal norm damping is applied for regularization, and we adopt PREM as the reference model. Since we do not invert for seismic velocity in the crust, prior to the inversions we correct all the data using crustal corrections from the model CRUST2.0. Therefore, our strategy to deal with the crust is a hybrid one; first, we carry out crustal corrections using CRUST2.0 taking into account crustal velocity and crustal thickness. Then, in our inversions, we estimate crustal thickness perturbations from CRUST2.0 using our data sets, which include group velocity data. The crustal thickness perturbations are estimated simultaneously to variations in 3-D shear wave velocity and radial anisotropy in the whole mantle. This is different from the strategy taken in the construction of e.g., models SEMum (Lekić and Romanowicz, 2011) and SEMum2 (French et al., 2013), in which group velocity data are used to build a crustal model without using existing a-priori crustal models. Moreover, we use group velocity data with a period range down to 16 s, while group velocity data down to 25 s are used in SEMum and SEMum2.

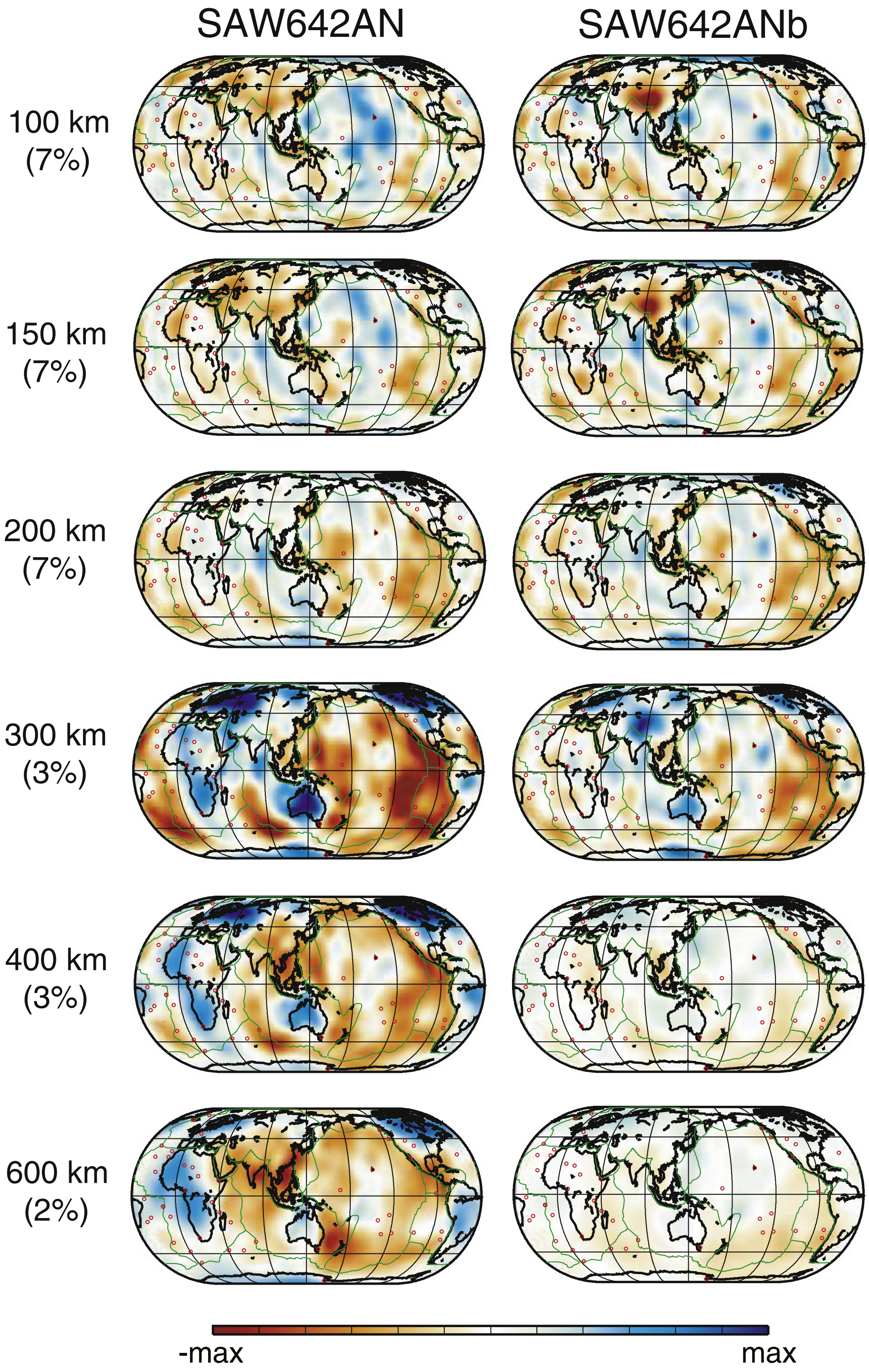

Fig. 11. Comparison between SAW642AN (Panning and Romanowicz, 2006) and SAW642ANb (Panning et al., 2010), which are built with the same datasets, parameterization, and crustal model (CRUST2.0), but with different crustal corrections. Please see the texts for details.

Fig. 14 shows the resolved Moho depth perturbations from CRUST2.0. Interestingly, the Moho depth is perturbed in oceanic crusts, which is commonly assumed to have a homogeneous thickness. The variations in oceanic crust seem larger than in continental crusts. Along subduction zones in the western Pacific, the resolved Moho is deeper than in CRUST2.0. The thicker crust may be reasonable since two oceanic crusts are superposing along the subduction zones. The continental crust beneath Pamir and Tibet is also thicker than in CRUST2.0, but the low crustal velocity beneath Tibet (e.g., Owens and Zandt, 1997) might have been mapped into the Moho perturbations. Indeed, crustal thickness estimates may be biased by trade-offs between crustal velocity and thickness.

In Figs. 15 and 16, we present depth slices of our preliminary whole mantle 3-D V_S isotropic and radially anisotropic models. The isotropic model in Fig. 15 shows common characteristic features found in previous 3-D global S-velocity models such as high-velocity anomalies beneath cratons at 100–200 km depth, low-velocity anomalies along ridges at 100 km depth, high-velocity anomalies at the mantle transition

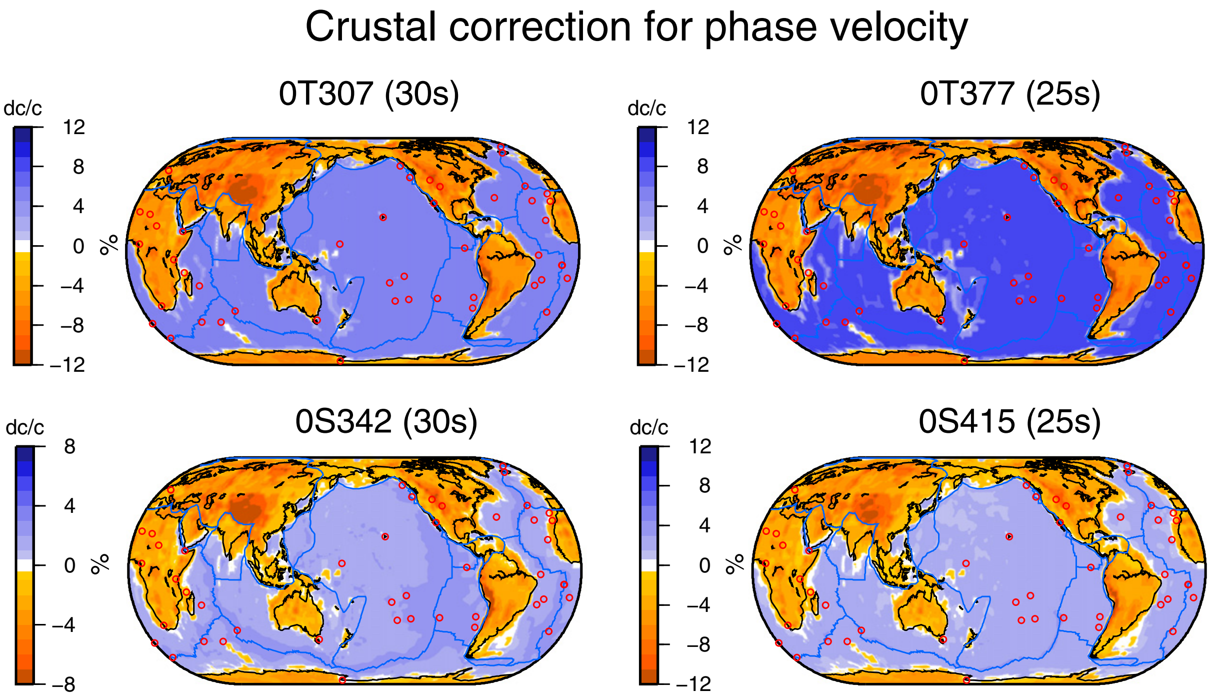

Fig. 12. Crustal corrections for fundamental-mode phase velocities. Crustal corrections for Love waves with periods of 30 and 25 s are shown on top, and corrections for Rayleigh waves with periods of 30 and 25 s are presented on the bottom.

zone beneath the western Pacific and Andes representing subducting slabs, and strong low-velocity anomalies in the two LLSVPs at 2800 km depth.

Compared with the previous 3-D anisotropic models shown in Fig. 3, our anisotropic model in Fig. 16 seems to be more consistent with the regional features explained in Section 5. For example, at a depth of 150 km, faster *SH* velocity is observed with large amplitude beneath the central Pacific, which is consistent with the regional observations discussed in Section 5.1. Along the East Pacific Rise, there is change in polarity of radial anisotropy from 100 to 250 km from faster *SH* velocity to faster *SV* velocity, which was also discussed in Section 5.2. Beneath continental crust at 250 km depth, faster *SH* velocity is observed in our model, which is consistent with mantle flow at the LAB. Our model shows weaker radial anisotropy in the lower mantle than

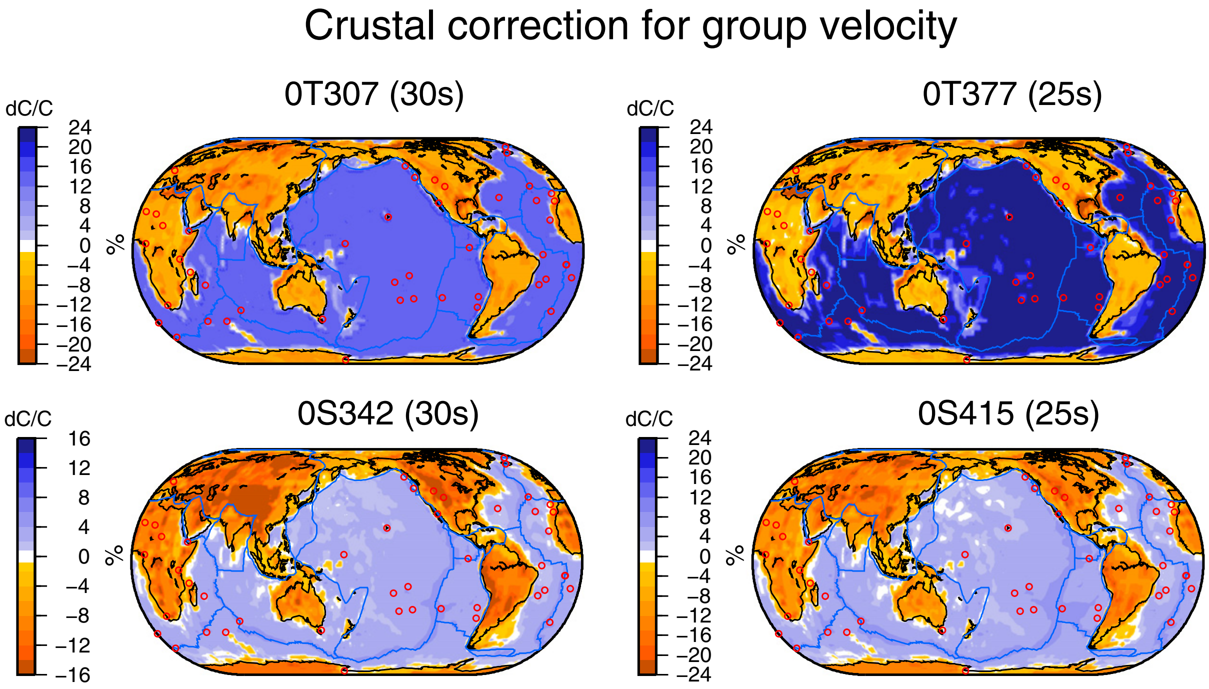

Fig. 13. Crustal corrections for fundamental-mode group velocities. Crustal corrections for Love waves with periods of 30 and 25 s are shown on top, and corrections for Rayleigh waves with periods of 30 and 25 s are presented on the bottom. Note that the scale bars span a range twice that used to plot crustal corrections for phase velocities in Fig. 12.

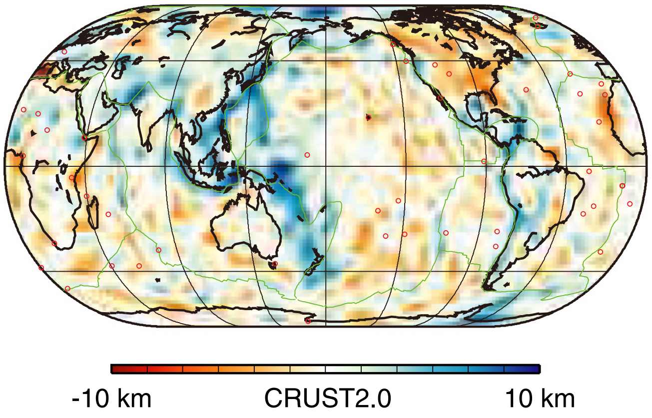

Fig. 14. Moho depth perturbations from CRUST2.0 (Bassin et al., 2000) from our inversions (see main text for details).

S362WMANI, but stronger than SAW642ANb. In D″, our model shows two distinct faster *SV* velocities inside the LLSVPs.

8.3. Trade-off between isotropic and anisotropic structure

Constraining radial anisotropy may also be hampered by trade-offs between isotropic heterogeneities and anisotropic structure. Anderson and Dziewoński (1982) showed that a low-velocity zone in the upper mantle resolved using an isotropic inversion disappears in a model derived by an anisotropic inversion with the same data. Kustowski et al. (2008) also demonstrated a clear trade-off between isotropic heterogeneities and anisotropic structure in the D″ region. We test this trade-off by performing an inversion for isotropic and anisotropic structure with an input model that consists of only the isotropic part of our model (i.e., the only anisotropy in the input model is that in the PREM starting model). The results are presented in Fig. 17, where from left to right we show: (a) the input model; (b) the anisotropic part of the output model, showing that in the D″ region the isotropic structure leaked into the anisotropic model; and, (c) the anisotropic part of our new preliminary 3-D Earth model. Although the amplitude of the anomalies in the resolved model (b) is smaller than in our anisotropic model (c), the pattern of radial anisotropy is similar. This implies that at least some portion of our D″ anisotropic model may be due to leaking of isotropic structure. This test reveals the difficulty in constraining global radial anisotropy in the D″ with current datasets. In order to reduce these trade-offs, larger and more varied datasets with better coverage are needed. Albeit this trade-off between isotropic and anisotropic structure, the radial anisotropy distribution in D″ obtained in the global tomographic inversions still matches observations of shear-wave splitting data with phases such as ScS and Sdiff (Fouch et al., 2001; Kendall and Silver, 1996; Lay and Helmberger, 1983; Lay and Young, 1991; Pulliam and Sen, 1998; Ritsema, 2000; Russell et al., 1998; Ritsema et al., 1998; Vinnik et al., 1995, 1998).

8.4. Limitations in methodology

As discussed in Section 2, in traditional tomography, the great-circle approximation is usually used to estimate 1-D average source-receiver kernels, neglecting the effects of 3-D structure along the great circle as well as off-propagation plane anomalies. With the growth of computational capacity, it is becoming possible to build radially anisotropic earth models using accurate purely numerical forward modeling schemes such as the Spectral Element Method (SEM; Komatitsch and Tromp, 2002a,b) and to calculate 3-D kernels for 3-D reference models (Tromp et al., 2005). Lekić and Romanowicz (2011) and French et al. (2013) applied a coupled SEM technique (Capdeville et al., 2003) to global tomography, but they use an approximate approach to correct for the crust and 2-D kernels. Bozdağ et al. (2012) are pushing SEM-based adjoint methods forward towards global tomographic inversions

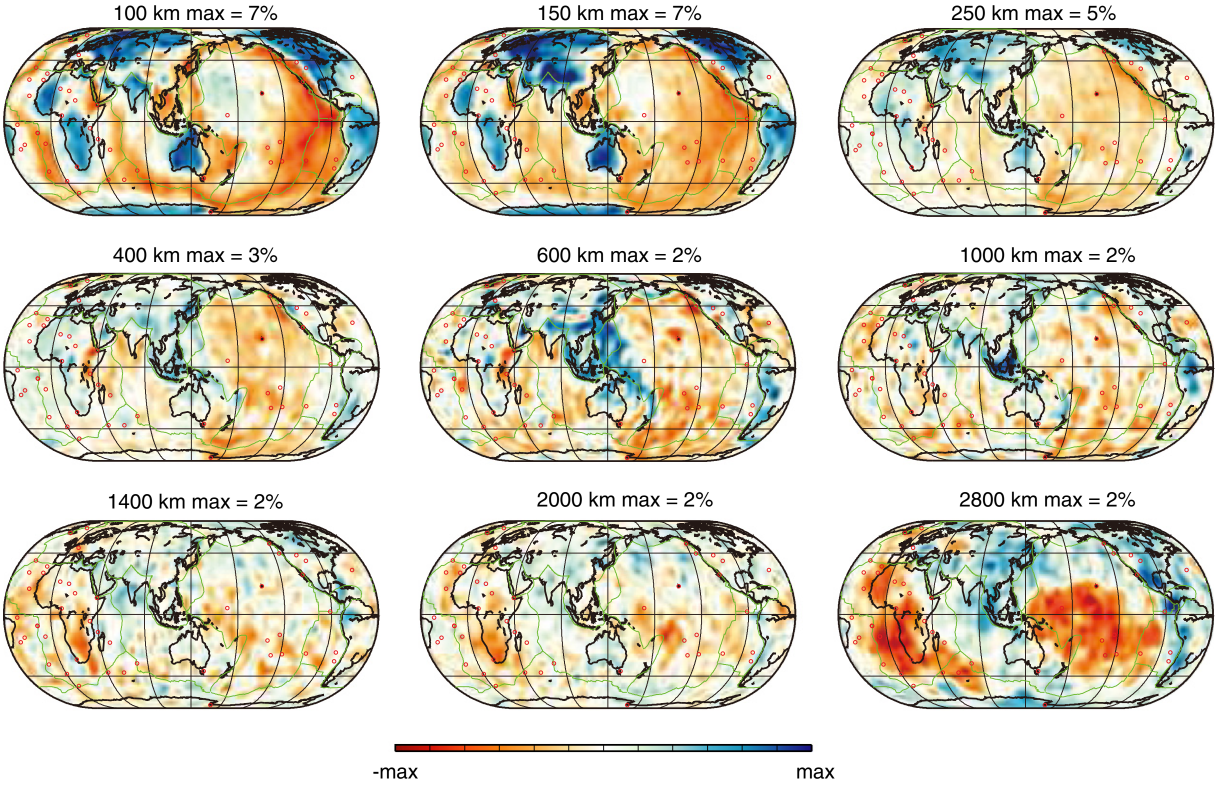

Fig. 15. Depth slicesc of our isotropic model at 100, 150, 250, 400, 600, 1000, 1400, 2000, and 2800 km from the preliminary isotropic model with multiple datasets.

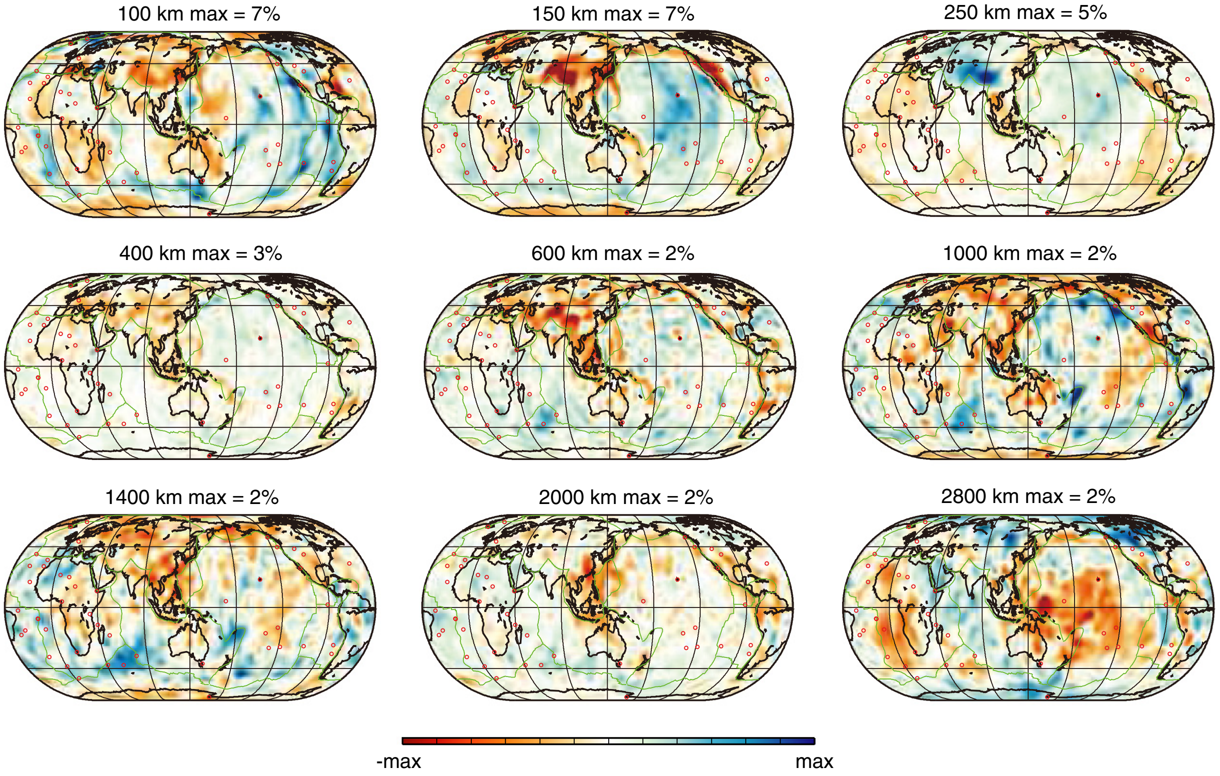

Fig. 16. Depth slices of our anisotropic model at 100, 150, 250, 400, 600, 1000, 1400, 2000, and 2800 km from the preliminary anisotropic model with multiple datasets. Scales at each depth are exactly the same as in Fig. 3 for convenience in comparison.

for mantle as well as crust simultaneously without any crustal corrections. However, this technique is still computationally very expensive, and only partly accounts for rapid variations of crustal structure at the continent–ocean boundaries by smoothing the variations.

Another issue is the use of scaling relationships for parameters such as perturbations in *P* velocity, *P* radial anisotropy, and density with respect to isotropic *S* velocity and *S* anisotropy perturbations in order to reduce the model parameters in the inversions. These parameters do not necessarily vary proportionally to isotropic *S* velocity and *S* anisotropy at all depths and may show also lateral variations (e.g., Ishii and Tromp, 1999; Masters et al., 2000). More accurate constraints from other disciplines such as mineral physics are needed to address these issues.

9. Conclusions and suggestions

Radial anisotropy can potentially play a role as a proxy for mantle convection via relationships between deformation represented as LPO and/or SPO and the resulting anisotropy. Since the 1960s, radial anisotropy in the mantle has been extensively recognized and studied, but still global 3-D anisotropic models are far from consensus, compared to the extent of consensus on 3-D global isotropic structure. Issues such as contamination by crustal structure, trade-offs between isotropic and anisotropic properties, and limitations in methods are hindering progress in global anisotropic imaging.

Furthermore, despite recent progress in linking seismic observations of radial anisotropy with information from mineral physics, there is still a lack of agreement in experiments for LPO of some minerals, which makes it difficult to interpret seismic observations straightforwardly in terms of mantle convection. We still only have relatively few experimental results for lower mantle minerals in high temperature and pressure simultaneously. In addition, radial anisotropy in the mantle transition zone is still poorly understood, with previous seismological studies showing different polarities of anisotropy in this region (see Fig. 2). Interpretations of anisotropy in this region are difficult since wadsleyite has different deformation directions according to water

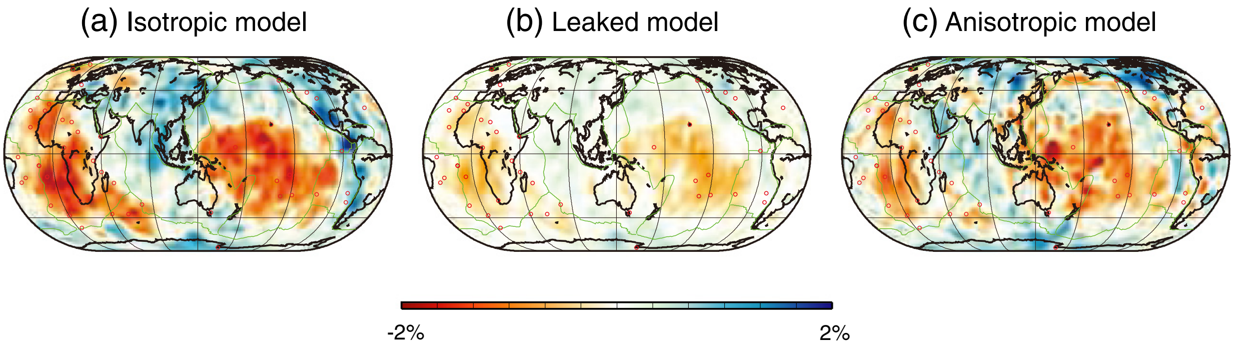

Fig. 17. Synthetic test to investigate trade-offs between isotropic heterogeneities and radial anisotropy in the lowermost mantle. (a) The preliminary isotropic model as the input model. (b) The anisotropic part of the output model from our synthetic inversion. (c) The anisotropic part of our new preliminary model.

content (Tommasi et al., 2004; Kawazoe et al., 2013; see Section 3.2). Towards the bottom of the transition zone, mechanisms to generate SPO are still needed to be understood, given that one of the dominant minerals here – ringwoodite – is thought to be nearly isotropic.

In this study, we presented a new radially anisotropic whole-mantle model by inverting surface-wave phase/group velocity measurements and body-wave travel time data. We added Moho perturbations as model parameters to the inversions in order to reduce the mapping of crustal effects into the mantle. The estimated Moho perturbations show thicker crust along the subduction zones beneath the western Pacific, which seems to show the superposition of two oceanic crusts along the subduction zones. The isotropic model from the inversion shares common features with previous 3-D *S*-velocity models, such as high-velocity anomalies beneath cratons and subduction zones. The anisotropic model shows some similarities with previous global 3-D models, and, importantly, seems to be more consistent with various persistent features in previous regional studies of radial anisotropy.

We now make some suggestions to improve the robustness of global 3-D radial anisotropy estimates. Above all, better data coverage and multiple datasets are required. On the one hand, it is important to continue expanding the global seismic network, especially by installing further ocean bottom seismometers to increase coverage over oceans. On the other hand, as shown in this study, the combination of massive complementary datasets is a key step. In particular, group-velocity data, which have not been used extensively in the estimation of global radial anisotropy (e.g., French et al., 2013; Lekić and Romanowicz, 2011; Shapiro and Ritzwoller, 2002), are very useful to jointly model anisotropy and crustal structure, avoiding the need to rely on approximate crustal corrections. In addition, ambient noise short-period group velocities (e.g., Shapiro et al., 2005) may also provide additional constraints on crustal structure.

Advanced methodologies are required for the three challenging tasks mentioned below. First, it will be important to calculate 3-D kernels with respect to radial anisotropy based on 3-D anisotropic reference models. By doing this, we could potentially resolve realistic amplitudes of anisotropic anomalies with better accuracy. Secondly, further efforts should focus on inversions for realistic crustal structure with sharp boundaries between the continents and the oceans in joint inversions for mantle and crustal structure, in order to further reduce the effect of the crust on mantle tomography. Thirdly, further studies should investigate other model parameters such as azimuthal anisotropy and *P* anisotropy and their impact on the inversions. Adjoint tomography may be a promising technique to accomplish all requirements aforementioned, but it still involves a very heavy computational burden.

In spite of all endeavors we mentioned above, ultimately it might be still difficult to constrain and interpret radial anisotropy only with seismic data. Additional data and constraints such as experimental results and simulations from mineral physics and geodynamics must be used to constrain the various parameters. By combining seismological approaches with information from other disciplines, radial anisotropy might be robustly estimated with less uncertainty.

Acknowledgments

We thank Timothy Horscroft and Hans Thybo from Tectonophysics for inviting us to write this review paper. We also thank Barbara Romanowicz and Shun-Ichiro Karato for their detailed and encouraging reviews, which improved our manuscript much. This research was supported by the Leverhulme Trust and was carried out on the High Performance Computing Cluster supported by the Research and Specialist Computing Support services at the University of East Anglia. Chris Collins is particularly thanked for assistance with our ceaseless requests for parallel processing. AMGF also thanks funding by the European Commission's Initial Training Network project QUEST (contract FP7-PEOPLE-ITN-2008-238007, www.quest-itn.org). This study was also supported by 2013 Research Grant from Kangwon National University. We gratefully acknowledge the availability of global seismograms from the IRIS/IDA/USGS, GEOSCOPE and GEOFON networks and the IRIS DATA Centre.

References

Aki, K., Kaminuma, K., 1963. Phase velocity of Love waves in Japan (part 1): love waves from the Aleutian shock of March 1957. Bull. Earthquake Res. Inst. 41, 243–259.

Aki, K., Richards, P.G., 1980. Quantitative Seismology, Theory and Methods. , vol. 1. W. H. Freeman and Company, San Francisco.

Aki, K., Christoffersson, A., Husebye, E.S., 1977. Determination of the 3-dimensional seismic structure of the lithosphere. J. Geophys. Res. 82, 277–296.

Anderson, D.L., 1961. Elastic wave propagation in layered anisotropic media. J. Geophys. Res. 66, 2953–2963.

Anderson, D.L., 1965. Recent evidence concerning the structure and composition of the Earth's mantle. Phys. Chem. Earth 6, 1–131.

Anderson, D.L., Dziewoński, A.M., 1982. Upper mantle anisotropy: evidence from free oscillations. Geophys. J. R. Astron. Soc. 69, 383–404.

Anderson, D.L., Spetzler, H., 1970. Partial melting and the low-velocity zone. Phys. Earth Planet. Inter. 4, 62–64.

Anderson, O.L., Schreiber, E., Liebermann, R.C., Soga, N., 1968. Some elastic constant data on minerals relevant to geophysics. Rev. Geophys. 6, 491–524.

Backus, G.E., 1962. Long-wave elastic anisotropy produced by horizontal layering. J. Geophys. Res. 67, 4427–4440.

Bassin, C., Laske, G., Masters, G., 2000. The current limits of resolution for surface wave tomography in North America. EOS Trans. Am. Geophys. Union 81 (Fall Meeting Supplement, Abstract S12A-03).

Becker, T.W., Kustowski, B., Ekström, G., 2008. Radial seismic anisotropy as a constraint for upper mantle rheology. Earth Planet. Sci. Lett. 267, 213–227.

Beghein, C., Trampert, J., van Heijst, H.J., 2006. Radial anisotropy in seismic reference models of the mantle. J. Geophys. Res. 111, B02303. http://dx.doi.org/10.1029/2005JB003728.

Bozdağ, E., Trampert, J., 2008. On crustal corrections in surface wave tomography. Geophys. J. Int. 172, 1066–1082.

Bozdağ, E., Zhu, H., Peter, D.B., Tromp, J., 2012. Towards global adjoint tomography. Abstract S34B-08 presented at 2012 Fall Meeting, American Geophysical Union, San Francisco, California, 3–7 December.

Capdeville, Y., Chaljub, E., Vilotte, J.P., Montagner, J.P., 2003. Coupling the spectral element method with a modal solution for elastic wave propagation in global earth models. Geophys. J. Int. 152, 34–67.

Cara, M., Lévêque, J.J., 1988. Anisotropy of the asthenosphere: the higher mode data of the Pacific revisited. Geophys. Res. Lett. 15, 205–208.

Chang, S.-J., Ferreira, A.M.G., Ritsema, J.E., van Heijst, H.J., Woodhouse, J.H., 2012. Global radially anisotropic mantle structure from multiple datasets. Abstract S32B-06 presented at 2012 Fall Meeting, American Geophysical Union, San Francisco, California, 3–7 December.

Collins, M.D., Brown, J.M., 1998. Elasticity of an upper mantle clinopyroxene. Phys. Chem. Miner. 26, 7–13.

Couvy, H., Frost, D.J., Heidelbach, F., Nyilas, K., Ungár, T., Mackwell, S., Cordier, P., 2004. Shear deformation experiments of forsterite at 11 GPa–1400 °C in the multianvil apparatus. Eur. J. Mineral. 16, 877–889.

Debayle, E., Kennett, B.L.N., 2000. Anisotropy in the Australian upper mantle from Love and Rayleigh waveform inversion. Earth Planet. Sci. Lett. 184, 339–351.

Dziewoński, A.M., Anderson, D.L., 1981. Preliminary reference Earth model. Phys. Earth Planet. Inter. 25, 297–356.

Dziewoński, A.M., Hager, B.H., O'Connell, R.J., 1977. Large-scale heterogeneities in the lower mantle. J. Geophys. Res. 82, 239–255.

Ekström, G., Dziewoński, A.M., 1998. The unique anisotropy of the Pacific upper mantle. Nature 394, 168–172.

Ferreira, A.M.G., Woodhouse, J.H., Visser, K., Trampert, J., 2010. On the robustness of global radially anisotropic surface wave tomography. J. Geophys. Res. 115, B04313. http://dx.doi.org/10.1029/2009JB006716.

Fouch, M.J., Fischer, K.M., Wysession, M., 2001. Lowermost mantle anisotropy beneath the Pacific: imaging the ousrce of the Hawaiian plume. Earth Planet. Sci. Lett. 190, 167–180.

French, S., Lekić, V., Romanowicz, B., 2013. Waveform tomography reveals channeled flow at the base of the oceanic asthenosphere. Science 342, 227–230.

Garnero, E.J., Maupin, V., Lay, T., Fouch, M.J., 2004. Variable azimuthal anisotropy in Earth's lowermost mantle. Science 306, 259–261.

Gu, Y.J., Dziewoński, A.M., Ekström, G., 2003. Simultaneous inversion for mantle shear velocity and topography of transition zone discontinuities. Geophys. J. Int. 154, 559–583.

Gu, Y.J., Lerner-Lam, A.L., Dziewoński, A.M., Ekström, G., 2005. Deep structure and seismic anisotropy beneath the East Pacific Rise. Earth Planet. Sci. Lett. 232, 259–272.

Gung, Y., Panning, M., Romanowicz, B., 2003. Global anisotropy and the thickness of continents. Nature 422, 707–711.

Hess, R., 1964. Seismic anisotropy of the uppermost mantle under the oceans. Nature 203, 629–631.

Hirose, K., Fei, Y., Ma, Y., Mao, H.-K., 1999. The fate of subducted basaltic crust in the Earth's lower mantle. Nature 397, 53–56.

Holtzman, B.K., Kohlstedt, D.L., Zimmerman, M.E., Heidelbach, F., Hiraga, T., Hustoft, J., 2003. Melt segregation and strain partitioning: implications for seismic anisotropy and mantle flow. Science 301, 1227–1230.

Ishii, M., Tromp, J., 1999. Normal-mode and free-air gravity constraints on lateral variations in velocity and density of Earth's mantle. Science 285, 1231–1236.

Jung, H., Karato, S.-I., 2001. Water-induced fabric transitions in olivine. Science 293, 1460–1463.

Karato, S.-I., 1988. The role of recrystallization in preferred orientation in olivine. Phys. Earth Planet. Inter. 51, 107–122.

Karato, S.-I., 1992. On the Lehmann discontinuity. Geophys. Res. Lett. 19, 2255–2258.

Karato, S.-I., 1997. On the separation of crustal component from oceanic lithosphere near the 660 km discontinuity. Phys. Earth Planet. Inter. 99, 103–111.

Karato, S.-I., 1998a. Seismic anisotropy in the deep mantle, boundary layers and the geometry of mantle convection. Pure Appl. Geophys. 151, 565–587.

Karato, S.-I., 1998b. Some remarks on the origin of seismic anisotropy in the D″ layer. Earth Planets Space 50, 1019–1028.

Karato, S.-I., 2008. Insights into the nature of plume-asthenosphere interaction from central Pacific geophysical anomalies. Earth Planet. Sci. Lett. 274, 234–240.

Karato, S.-I., 2012. On the origin of the asthenosphere. Earth Planet. Sci. Lett. 321–322, 95–103.

Karato, S.-I., Zhang, S., Wenk, H.-R., 1995. Superplasticity in the Earth's lower mantle: evidence from seismic anisotropy and mineral physics. Science 270, 458–461.

Karato, S.-I., Jung, H., Katayama, I., Skemer, P., 2008. Geodynamic significance of seismic anisotropy of the upper mantle: new insights from laboratory studies. Annu. Rev. Earth Planet. Sci. 36, 59–95.

Karki, B.B., Stixrude, L., Clark, S.J., Warren, M.C., Ackland, G.J., Crain, J., 1997. Structure and elasticity of MgO at high pressure. Am. Mineral. 82, 51–60.

Kawai, K., Geller, R.J., 2010. The vertical flow in the lowermost mantle beneath the Pacific from inversion of seismic waveforms for anisotropic structure. Earth Planet. Sci. Lett. 297, 190–198.

Kawakatsu, H., Kumar, P., Takei, Y., Shinohara, M., Kanazawa, T., Araki, E., Suyehiro, K., 2009. Seismic evidence for sharp lithosphere–asthenosphere boundaries of oceanic plates. Science 324, 499–502.

Kawazoe, T., Ohuchi, T., Nishihara, Y., Nishiyama, N., Fujino, K., Irifune, T., 2013. Seismic anisotropy in the mantle transition zone induced by shear deformation of wadsleyite. Phys. Earth Planet. Inter. 216, 91–98.

Kendall, J.-M., 2000. Seismic anisotropy in the boundary layers of the mantle. In: Karato, S.-I., Forte, A.M., Liebermann, R.C., Masters, G., Stixrude, L. (Eds.), Earth's Interior: Mineral Physics and Tomography from the Atomic to the Global Scale. Geophysical Monograph, 117. American Geophysical Union, Washington, D.C., USA, pp. 133–159.

Kendall, J.-M., Silver, P.G., 1996. Constraints from seismic anisotropy on the nature of the lowermost mantle. Nature 381, 409–412.

Kendall, J.-M., Silver, P.G., 1998. Investigating causes of D″ anisotropy. In: Gurnis, M., Wysession, M.E., Knittle, E., Buffett, B.A. (Eds.), The Core–Mantle Boundary Region. Geodynamics series, 28. American Geophysical Union, Washington, D.C., USA, pp. 97–118.

Kennett, B.L.N., Engdahl, E.R., 1991. Traveltimes for global earthquake location and phase identification. Geophys. J. Int. 105, 429–465.

Komatitsch, D., Tromp, J., 2002a. Spectral-element simulations of global seismic wave propagation—I. Validation. Geophys. J. Int. 149, 390–412.

Komatitsch, D., Tromp, J., 2002b. Spectral-element simulations of global seismic wave propagation—II. Three-dimensional models, oceans, rotation and self-gravitation. Geophys. J. Int. 150, 303–318.

Kumazawa, M., Anderson, D.L., 1969. Elastic moduli, pressure derivatives, and temperature derivatives of single-crystal olivine and single-crystal fosterite. J. Geophys. Res. 74, 5961–5972.

Kustowski, B., Dziewoński, A.M., Ekström, G., 2007. Nonlinear crustal corrections for normal-mode seismograms. Bull. Seismol. Soc. Am. 97, 1756–1762.

Kustowski, B., Ekström, G., Dziewoński, A.M., 2008. Anisotropic shear-wave velocity structure of the Earth's mantle: a global model. J. Geophys. Res. 113, B06306. http://dx.doi.org/10.1029/2007JB005169.

Lay, T., Helmberger, D., 1983. The shear-wave velocity-gradient at the base of the mantle. J. Geophys. Res. 88, 8160–8170.

Lay, T., Young, C., 1991. Analysis of seismic SV waves in the core's penumbra. Geophys. Res. Lett. 18, 1373–1376.

Lebedev, S., Adam, J.M.-C., Meier, T., 2013. Mapping the Moho with seismic surface waves: a review, resolution analysis, and recommended inversion strategies. Tectonophysics. http://dx.doi.org/10.1016/j.tecto.2012.12.030.

Lekić, V., Romanowicz, B., 2011. Inferring upper-mantle structure by full waveform tomography with the spectral element method. Geophys. J. Int. 185, 799–831.

Lekić, V., Panning, M., Romanowicz, B., 2010. A simple method for improving crustal corrections in waveform tomography. Geophys. J. Int. 182, 265–278.

Levien, L., Weidner, D.J., Prewitt, C.T., 1979. Elasticity of diopside. Phys. Chem. Miner. 4, 105–113.

Li, X.-D., Romanowicz, B., 1996. Global mantle shear velocity model developed using nonlinear asymptotic coupling theory. J. Geophys. Res. 101, 22,245–22,272.

Li, L., Weidner, D.J., Brodholt, J., Alfé, D., Price, G.D., Caracas, R., Wentzcoitch, R., 2006. Elasticity of $CaSiO_3$ perovskite at high pressure and high temperature. Phys. Earth Planet. Inter. 155, 249–259.

Long, M.D., 2013. Constraints on subduction geodynamics from seismic anisotropy. Rev. Geophys. 51, 76–112.

Love, A.E.H., 1927. A Treatise on the Theory of Elasticity. Cambridge University Press, Cambridge.

Mainprice, D., 2007. Seismic anisotropy of the deep Earth from a mineral and rock physics perspective. In: Schubert, G. (Ed.), Treatise on Geophysics. , vol. 2. Elsevier, Oxford, UK, pp. 437–492.

Mainprice, D., Barruol, G., Ben Ismaïl, W., 2000. The seismic anisotropy of the Earth's mantle: from single crystal to polycrystal. In: Karato, S.-I., Forte, A.M., Liebermann, R.C., Masters, G., Stixrude, L. (Eds.), Earth's Interior: Mineral physics and tomography from the atomic to the global scale. Geophysical Monograph, 117. American Geophysical Union, Washington, D.C., USA, pp. 237–264.

Mainprice, D., Tommasi, A., Couvy, H., Cordier, P., Frost, D.J., 2005. Pressure sensitivity of olivine slip systems and seismic anisotropy of Earth's upper mantle. Nature 433, 731–733.

Mainprice, D., Tommasi, A., Ferre, D., Carrez, P., Cordier, P., 2008. Predicted glide systems and crystal preferred orientations of polycrystalline silicate Mg-Perovsikte at high pressure: implications for the seismic anisotropy in the lower mantle. Earth Planet. Sci. Lett. 271, 135–144.

Mao, W.L., Meng, Y., Mao, H., 2010. Elastic anisotropy of ferromagnesian post-perovskite in Earth's D″ layer. Phys. Earth Planet. Inter. 180, 203–208.

Marone, F., Romanowicz, B., 2007. Non-linear crustal corrections in high-resolution regional waveform seismic tomography. Geophys. J. Int. 170, 460–467.

Marquardt, H., Speziale, S., Reichmann, H.J., Frost, D.J., Schilling, F.R., Garnero, E.J., 2009. Elastic shear anisotropy of ferropericlase in Earth's lower mantle. Science 324, 224–226.

Masters, G., Laske, G., Bolton, H., Dziewoński, A., 2000. The relative behavior of shear velocity, bulk sound speed, and compressional velocity in the mantle: implications for chemical and thermal structure. In: Karato, S.-I., Forte, A.M., Liebermann, R.C., Masters, G., Stixrude, L. (Eds.), Earth's Interior: Mineral Physics and Tomography from the Atomic to the Global Scale. Geophysical Monograph, 117. American Geophysical Union, Washington, D.C., USA, pp. 63–87.

Maupin, V., Garnero, E.J., Lay, T., Fouch, M.J., 2005. Azimuthal anisotropy in the D″ layer beneath the Caribbean. J. Geophys. Res. B08301. http://dx.doi.org/10.1029/2004JB003506.

McEvilly, T.V., 1964. Central U.S. crust–upper mantle structure from Love and Rayleigh wave phase velocity inversion. Bull. Seismol. Soc. Am. 54, 1997–2015.

Meier, U., Curtis, A., Trampert, J., 2007. Fully nonlinear inversion of fundamental mode surface waves for a global crustal model. Geophys. Res. Lett. 34, L16304. http://dx.doi.org/10.1029/2007GL030989.

Merkel, S., Kubo, A., Miyagi, L., Speziale, S., Duffy, T.S., Mao, H.-K., Wenk, H.-R., 2006. Plastic deformation of $MgGeO_3$ post-perovskite at lower mantle pressures. Science 311, 644–646.

Merkel, S., McNamara, A.K., Kubo, A., Speziale, S., Miyagi, L., Meng, Y., Duffy, T.S., Wenk, H.R., 2007. Deformation of (Mg, Fe)SiO_3 post-perovskite and D″ anisotropy. Science 316, 1729–1732.

Miyagi, L., Kanitpanyacharoen, W., Kaercher, P., Lee, K.K.M., Wenk, H.R., 2010. Slip systems in $MgSiO_3$ post-perovskite: implication for D″ anisotropy. Science 329, 1639–1641.

Miyazaki, T., Sueyoshi, K., Hiraga, T., 2013. Olivine crystals align during diffusion creep of Earth's upper mantle. Nature 502, 321–326.

Montagner, J.-P., 1998. Where can seismic anisotropy be detected in the Earth's mantle? In boundary layers. Pure Appl. Geophys. 151, 223–256.

Montagner, J.-P., Anderson, D.L., 1989a. Petrological constraints on seismic anisotropy. Phys. Earth Planet. Inter. 54, 82–105.

Montagner, J.-P., Anderson, D.L., 1989b. Constrained reference mantle model. Phys. Earth Planet. Inter. 58, 205–227.

Montagner, J.-P., Kennett, B.L.N., 1996. How to reconcile body-wave and normal-mode reference Earth models. Geophys. J. Int. 125, 229–248.

Montagner, J.-P., Tanimoto, T., 1991. Global upper mantle tomography of seismic velocities and anisotropies. J. Geophys. Res. 96, 20337–20351.

Montelli, R., Nolet, G., Dahlen, F.A., Masters, G., Engdahl, E.R., Hung, S.-H., 2004. Finite-frequency tomography reveals a variety of plumes in the mantle. Science 303, 338–343.

Murakami, M., Hirose, K., Kawamura, K., Sata, N., Ohishi, Y., 2004. Post-perovskite phase transition in $MgSiO_3$. Science 304, 855–857.

Nataf, H.-C., Ricard, Y., 1996. 3SMAC: an a priori tomographic model of the upper mantle based on geophysical modeling. Phys. Earth Planet. Inter. 95, 101–122.

Nataf, H.-C., Nakanishi, I., Anderson, D.L., 1984. Anisotropy and shear-velocity heterogeneities in the upper mantle. Geophys. Res. Lett. 11, 109–112.

Nataf, H.-C., Nakanishi, I., Anderson, D.L., 1986. Measurements of mantle wave velocities and inversion for lateral heterogeneities and anisotropy 3. Inversion. J. Geophys. Res. 91, 7261–7307.

Nicolas, A., Christensen, N.I., 1987. Formation of anisotropy in upper mantle peridotites: a review. In: Fuchs, K., Froidevaux, C. (Eds.), Composition, Structure and Dynamics of the Lithosphere–Asthenosphere System. Geodynamics series, 16. American Geophysical Union, Washington, D.C., USA, pp. 111–123.

Nishimura, C.E., Forsyth, D.W., 1989. The anisotropic structure of the upper mantle in the Pacific. Geophys. J. R. Astron. Soc. 63, 497–514.

Nowacki, A., Wookey, J., Kendall, J.-M., 2010. Deformation of the lowermost mantle from seismic anisotropy. Nature 467, 1091–1094.

Nowacki, A., Wookey, J., Kendall, J.-M., 2011. New advances in using seismic anisotropy, mineral physics and geodynamics to understand deformation in the lowermost mantle. J. Geodyn. 52, 205–228.

Oganov, A.R., Ono, S., 2004. Theoretical and experimental evidence for a post-perovskite phase of $MgSiO_3$ in Earth's D″ layer. Nature 430, 445–448.

Oganov, A.R., Brodholt, J.P., Price, G.D., 2001. The elastic constants of $MgSiO_3$ perovskite at pressures and temperatures of the earth's mantle. Nature 411, 934–937.

Ohuchi, T., Irifune, T., 2013. Development of A-type olivine fabric in water-rich deep upper mantle. Earth Planet. Sci. Lett. 362, 20–30.

Owens, T.J., Zandt, G., 1997. Implications of crustal property variations for models of Tibetan plateau evolution. Nature 387, 37–43.

Panning, M., Romanowicz, B., 2004. Inferences on flow at the base of the Earth's mantle based on seismic anisotropy. Science 303, 351–353.

Panning, M., Romanowicz, B., 2006. A three-dimensional radially anisotropic model of shear velocity in the whole mantle. Geophys. J. Int. 167, 361–379.

Panning, M.P., Lekić, V., Romanowicz, B., 2010. Importance of crustal corrections in the development of a new global model of radial anisotropy. J. Geophys. Res. 115, B12325. http://dx.doi.org/10.1029/2010JB007520.

Pulliam, J., Sen, M.K., 1998. Seismic anisotropy in the core–mantle transition zone. Geophys. J. Int. 135, 113–128.

Ritsema, J., 2000. Evidence for shear velocity anisotropy in the lowermost mantle beneath the Indian Ocean. Geophys. Res. Lett. 27, 1041–1044.

Ritsema, J., Lay, T., Garnero, E.J., Benz, H., 1998. Seismic anisotropy in the lowermost mantle beneath the Pacific. Geophys. Res. Lett. 25, 1229–1232.

Ritsema, J., van Heijst, H.J., Woodhouse, J.H., 2004. Global transition zone tomography. J. Geophys. Res. 109, B02302. http://dx.doi.org/10.1029/2003JB002610.

Ritsema, J., Deuss, A., van Heijst, H.J., Woodhouse, J.H., 2011. S40RTS: a degree-40 shear-velocity model for the mantle from new Rayleigh wave dispersion, teleseismic traveltime and normal-mode splitting function measurements. Geophys. J. Int. 184, 1223–1236.

Ritzwoller, M.H., Levshin, A.L., 1998. Eurasian surface wave tomography: group velocities. J. Geophys. Res. 103, 4839–4878.

Robertson, G.S., Woodhouse, J.H., 1995. Evidence for proportionality of P and S heterogeneity in the lower mantle. Geophys. J. Int. 123, 85–116.

Russell, S.A., Lay, T., Garnero, E.J., 1998. Seismic evidence for small-scale dynamics in the lowermost mantle at the root of the Hawaiian hotspot. Nature 396, 255–258.

Savage, M.K., 1999. Seismic anisotropy and mantle deformation: what have we learned from shear wave splitting? Rev. Geophys. 37, 65–106.

Shapiro, N.M., Ritzwoller, M.H., 2002. Monte-Carlo inversion for a global shear-velocity model of the crust and upper mantle. Geophys. J. Int. 151, 88–105.

Shapiro, N.M., Campillo, M., Stehly, L., Ritzwoller, M.H., 2005. High-resolution surface-wave tomography from ambient seismic noise. Science 307, 1615–1618.

Silver, P.G., 1996. Seismic anisotropy beneath the continents: probing the depths of geology. Annu. Rev. Earth Planet. Sci. 24, 385–432.

Takeuchi, H., Saito, M., 1972. Seismic surface waves. In: Bolt, B.A. (Ed.), Methods of Computational Physics, vol. 11. Academic Press, New York, pp. 217–295.

Tommasi, A., Mainprice, D., Cordier, P., Thoraval, C., Couvy, H., 2004. Strain-induced seismic anisotropy of wadsleyite polycrystals and flow patterns in the mantle transition zone. J. Geophys. Res. 109, B12405. http://dx.doi.org/10.1029/2004JB003158.

Tromp, J., Tape, C., Liu, Q., 2005. Seismic tomography, adjoint methods, time reversal and banana–doughnut kernels. Geophys. J. Int. 160, 195–216.

Vinnik, L.P., Romanowicz, B., Stunff, Y.L., Makeyeva, L., 1995. Seismic anisotropy in the D″ layer. Geophys. Res. Lett. 22, 1657–1660.

Vinnik, L.P., Breger, L., Romanowicz, B., 1998. Anisotropic structures at the base of the Earth's mantle. Nature 393, 564–567.

Visser, K., Trampert, J., Lebedev, S., Kennett, B.L.N., 2008. Probability of radial anisotropy in the deep mantle. Earth Planet. Sci. Lett. 270, 241–250.

Webb, S.C., Forsyth, D.W., 1998. Structure of the upper mantle under the EPR from waveform inversion of regional events. Science 280, 1227–1229.

Webb, S.L., Jackson, I., 1993. The pressure dependence of the elastic moduli of single-crystal orthopyroxene ($Mg_{0.8}Fe_{0.2}$)SiO_3. Eur. J. Mineral. 5, 1111–1119.

Weidner, D.J., Wang, H., Ito, J., 1978. Elasticity of orthoenstatite. Phys. Earth Planet. Inter. 17, P7–P13.

Weidner, D.J., Sawamoto, H., Sasaki, S., Kumazawa, M., 1984. Single-crystal elastic properties of the spinel phase of Mg_2SiO_4. J. Geophys. Res. 89, 7852–7860.

Wenk, H.-R., Cottaar, S., Tome, C.N., McNamara, A., Romanowicz, B., 2011. Deformation in the lowermost mantle: from polycrystal plasticity to seismic anisotropy. Earth Planet. Sci. Lett. 308, 33–45.

Wentzcovitch, R.M., Karki, B.B., Cococcioni, M., de Gironcoli, S., 2004. Thermoelastic properties of $MgSiO_3$ perovskite: insights on the nature of the Earth's lower mantle. Phys. Rev. Lett. 92, 018501.

Wolfe, C.J., Solomon, S.C., 1998. Shear-wave splitting and implications for mantle flow beneath the MELT region of the East Pacific Rise. Science 280, 1230–1232.

Woodhouse, J.H., 1981. A note on the calculation of travel times in a transversely isotropic Earth model. Phys. Earth Planet. Inter. 25, 357–359.

Woodhouse, J.H., Dziewoński, A.M., 1984. Mapping the upper mantle; three-dimensional modeling of Earth structure by inversion of seismic waveforms. J. Geophys. Res. 89, 5953–5986.

Woodhouse, J.H., Girnius, T.P., 1982. The calculation of $d\Delta/dp$ and of partial derivatives for travel-time inversion in transversely isotropic spherical earth models. In Seismic Discrimination, Semiannual Technical Summary Report to the Defense Advanced Research Projects AgencyMassachusetts Institute of Technology, Lincoln Lab., Lexington, Massachusetts 61–65.

Wookey, J., Kendall, J.-M., 2007. Seismic anisotropy of post-perovskite and the lowermost mantle. In: Hirose, K., Brodholt, J., Lay, T., Yuen, D.A. (Eds.), Post-Perovskite: The Last Mantle Phase Transition. Geophysical Monograph, 174. American Geophysical Union, Washinton, D.C., USA, pp. 171–189.

Yamazaki, D., Karato, S.-I., 2002. Fabric development in (Mg, Fe)O during large strain, shear deformation: implications for seismic anisotropy in Earth's lower mantle. Phys. Earth Planet. Inter. 131, 251–267.

Yamazaki, D., Karato, S.-I., 2007. Lattice-preferred orientation of lower mantle materials and seismic anisotropy in the D″ layer. In: Hirose, K., Brodholt, J., Lay, T., Yuen, D.A. (Eds.), Post-Perovskite: The Last Mantle Phase Transition. Geophysical Monograph, 174. American Geophysical Union, Washinton, D.C., USA, pp. 171–189.

Yamazaki, D., Yoshino, T., Ohfuji, H., Ando, J.-I., Yoneda, A., 2006. Origin of seismic anisotropy in the D″ layer inferred from shear deformation experiments on post-perovskite phase. Earth Planet. Sci. Lett. 252, 372–378.

Yeganeh-Haeri, A., 1994. Synthesis and re-investigation of the elastic properties of single-crystal magnesium silicate perovskite. Phys. Earth Planet. Inter. 87, 111–121.

Zha, C.-S., Duffy, T.S., Mao, H.-K., Downs, R.T., Hemley, R.J., Weidner, D.J., 1997. Single-crystal elasticity of β-Mg_2SiO_4 to the pressure of the 410 km seismic discontinuity in the Earth's mantle. Earth Planet. Sci. Lett. 147, E9–E15.

Zhou, Y., 2009. Multimode surface wave sensitivity kernels in radially anisotropic earth media. Geophys. J. Int. 176, 865–888.

Zhou, Y., Nolet, G., Dahlen, F.A., Laske, G., 2006. Global upper-mantle structure from finite-frequency surface-wave tomography. J. Geophys. Res. 111, B04304. http://dx.doi.org/10.1029/2005JB003677.